

Cámara de prueba de CCDs para el experimento DAMIC-M.

(CCD Test Chamber Setup for DAMIC-M)

Trabajo de Fin de Máster para acceder al

MÁSTER EN FÍSICA DE PARTÍCULAS Y DEL COSMOS

Autor: Jazmin Morales Morales

Director\es: Rocío Vilar Cortabitarte

Amparo López Virto

Octubre 2020

Abstract

The aim of this thesis is to study the sources of damage in silicon sensors, in particular the ones dedicated to Charge Couples Devices (CCDs) at DAMIC and DAMIC-M. This work is made with the idea of future applications in the CCDs of the DAMIC-M (Dark Matter In CCDs at Modane) experiment in order to improve the performance of the Dark Matter search; to accomplish this objective, a review of the state of the art for the different techniques used for the treatment of such damage is done. Besides, a study of the dark current and its dependence on the temperature for real data obtained at DAMIC is included, observing a linear dependence at first instance.

Resumen

El propósito de este TFM es estudiar las fuentes de daño en detectores a base de silicón, en particular, aquellos dedicados a las CCDs (Charged Coupled Devices, en inglés) en los experimentos DAMIC y DAMIC-M. Este trabajo está hecho teniendo en cuenta las futuras aplicaciones en las CCDs del experimento DAMIC-M (Dark Matter In CCDs at Modane), para poder mejorar la búsqueda de materia oscura con este tipo de experimentos. Para cumplir este objetivo, se hace una revisión del estado del arte de las diferentes técnicas utilizadas para tratar dicho daño. Además, se hace un estudio de la corriente oscura y su dependencia con la temperatura para datos reales obtenidos en DAMIC, se observa que hay una dependencia linear en un primer análisis.

Acknowledgements

I would first like to thank my supervisors, Rocio Vilar and Amparo López, whose knowledge, expertise and kindness were fundamental in this thesis, mainly considering the difficult times we are facing due to the pandemics.

I would like to acknowledge our master coordinators, Patricio Vielva and Gervasio Gomez, your hard work and your attentions were very important during this program. To Carolina Foundation, for give me the opportunity of attend this master.

In addition, I would like to thank my family for the huge support you have been during all my formation years, you are the greatest gift I have.

Jazmin Morales Morales

0. Acknowledgements						
To my grandpa, for all your love and the many beautiful memories you left us.						

Contents

Al	Abstract Resumen Acknowledgements Contents					
Re						
A						
Co						
1	Introduction					
2	Darl	x Matte	r	3		
	2.1	Eviden	nce	3		
	2.2	Search	of Dark Matter: candidates	5		
		2.2.1	Direct detection	7		
3	Semiconductors					
	3.1	Silicon	Semiconductors as detectors	10		
		3.1.1	Silicon doping	12		
		3.1.2	Silicon Diode	14		
	3.2	Charge	ed Coupled Devices as Silicon semiconductors	16		
	3.3	Damag	ge in Silicon semiconductors	17		
		3.3.1	Crystal defects	18		
		3.3.2	Radiation damage	18		
		3.3.3	Characterisation of damage in semiconductors	20		
		3.3.4	Sources of noise in CCDs: Dark Current	20		
4	DAMIC and DAMIC-M					
	4.1	Experi	mental setup	23		
			5.1100.16			

0. Contents

5	Data analysis of the dark current							
	5.1	5.1 Test-stand CCDs at IFCA						
	5.2	5.2 Dark Current analysis						
		5.2.1 The FITS format	31					
		5.2.2 Overscan	31					
		5.2.3 Results	33					
6	Conclusions							
A	Search of Dark Matter: detection methods							
	A.1	Indirect detection	43					
	A.2	Search at accelerators	43					
В	Physics of semiconductors							
	B.1	The band structure	44					
C	DAMIC experimental setup							
	C.1	Readout	46					
D	D Expected results from DAMIC and DAMIC-M							
E	Test-stand CCDs at IFCA: current status							
Re	References							

Chapter 1

Introduction

The search of Dark Matter (DM) has been one of the main concerns of the scientific community since its existence was proposed, the detection and the measure of its properties could complete the actual cosmological paradigm; the success of some extensions to the Standard Model of Particle Physics rely on the existence of such type of matter, as well. There is a large number of candidates for DM, being WIMPs (Weakly Interactive Massive Particles) one of the most popular. Exhaustive efforts are made to detect the small interactions of Dark Matter candidates because, as the name suggests, this candidate interacts very weakly; hence it is fundamental to have meticulous measurements in the experimental arrangements.

The actual Standard Cosmological Model, or ΛCDM Model, proposes that the content of the Universe is 5% of baryonic matter, 27% of DM and 68% of Dark Energy [eaPC14]. Reaching to this assumption took almost 80 years, it was not until the 1930's when Zwicky and Smith found that the amount of mass observed in the Coma and Virgo clusters differed from the one computed by Hubble in 1926 [Pee93]. The idea of *missing mass* evolved into the actual model of Dark Matter, even nowadays its abundance can be measured from the CMB (Cosmic Microwave Background). Chapter 2 contains the description of this model, as well as a brief explanation of the different types of experimental search for DM: direct, indirect and search at accelerators.

The development of this TFM is based on a direct search experiment based in CCDs. The flow of this work will be conducted in the following way. In Chapter 3 the performance of semiconductors adopted as particle detectors is presented, in this work emphasis is put on the use of Silicon Charged Coupled Devices (CCDs). These devices are highly efficient particle detectors due to their sensitivity to ionized particles, for this reason CCDs are already employed in astronomical exploration and the search of Dark Matter (such as the Hubble Space Telescope or the Euclid mission and the DAMIC experiment, as it will be presented later; whereas silicon detectors are commonly utilized at CERN). For the correct operation of the experiments, it is mandatory to have a good understanding of the damage generated in the CCDs, knowing the origin of these issues allows to improve the actual technology; defects are mainly found at the surface and bulk of a CCD. Ionization radiation is one of the most common sources of surface damage, the consequences of which cause both an alteration in

1. Introduction

the energy distribution of interface defects and an increase in the defect density, which lead also to an increase in the surface dark current. In the case of bulk damage, vacancy defects are produced by the release of an atom in the lattice, this initial atom can displace further atoms. This section also provides a review of some techniques developed to treat the noise generated for such damage.

DAMIC is an underground experiment installed at SNOLAB in Canada at the end of 2012. It consists of an array of scientific CCDs that are fabricated from n-type silicon wafers. The CCDs detect the ionization produced for the recoil of a WIMP-nucleus elastic scattering; it is known for its high sensitivity to particles with mass below $10 \text{ GeV}/c^2$, a mass commonly associated to WIMPs. Chapter 4 presents a review of the main features of DAMIC experiment along with DAMIC-M (DAMIC at Mondane), a future detector planned to be installed at the Laboratoire Souterrain de Modane in France which uses the same technology as in DAMIC, but with the implementation of more massive CCDs, and where the control of dark current become crucial to obtain the desired sensitive.

The following chapter, Chapter 5, gives an example of how the images at DAMIC are obtained. The data collected is stored in a Flexible Image Transport System (FITS) format. The resulting CCD image gives information about the pixel position (x and y coordinates) and the pixel charge which represents the interaction of a particle with the atom in the silicon. One of the main problems in this type of direct search experiments is the background, which could be internal or external. The expected signal and rates are very small and any source of background could be misled. In particular, for this project, the attention is centered on the level of dark current in the system, one of the main sources of noise in CCDs.

Chapter 2

Dark Matter

The speculation of having matter in the universe which is "invisible to our eyes" has been present since ancient civilizations, the clearest example might be the approach of matter composed by elementary and indivisible blocks, or atoms, stated mainly by Democritus in the 5th century BCE. This idea evolved until the actual Standard Model of particle physics. Astronomical observations have showed a lack of matter in galaxies and galaxy clusters, in addition to some missing pieces in fundamental theories such as high energy physics and cosmology, have provided a proper scenario for a dark matter model.

In this chapter, a review of some of the main observational evidences are made followed by a set of suitable candidates for Dark Matter. At the end, the direct search of DM is described.

2.1 Evidence

In 1926 Hubble made an attempt to compute the mass of the Universe based on the total number of galaxies as well as the mass of each galaxy, the content of mass per galaxy was derived from the gravitational binding energies needed to contain the motions of stars and gas within galaxies [Pee93]. Hubble and Humason (1931) observed a larger scatter in the apparent velocities in the Coma cluster compared with other clusters.

It was in 1933 and 1936 that Zwicky and Smith, respectively, measured the velocity dispersion of galaxies content in the Coma and Virgo clusters, they noticed a missing fraction of mass when comparing with the Hubble predictions. For this situation, Zwicky decided to apply the virial theorem to the Coma cluster and calculate its mass. He found that the velocity dispersion should be of 80 km/s, but the observations showed an average velocity dispersion along the line of sight of 1000 km/s; from his observations he concluded that: "if this would be confirmed, we would get the surprising result that dark matter is present in much greater amount than luminous matter" [BH18].

The *rotation curve* of a galaxy shows the circular velocity profile of such galaxy as a function of the ratio to its center. From this curve it is possible to estimate the mass distribution of galaxies, for this reason its use played an important role in the discovery of dark matter. From Newtonian mechanics the mass M of the stars (i.e., the luminous mass of the disk) and

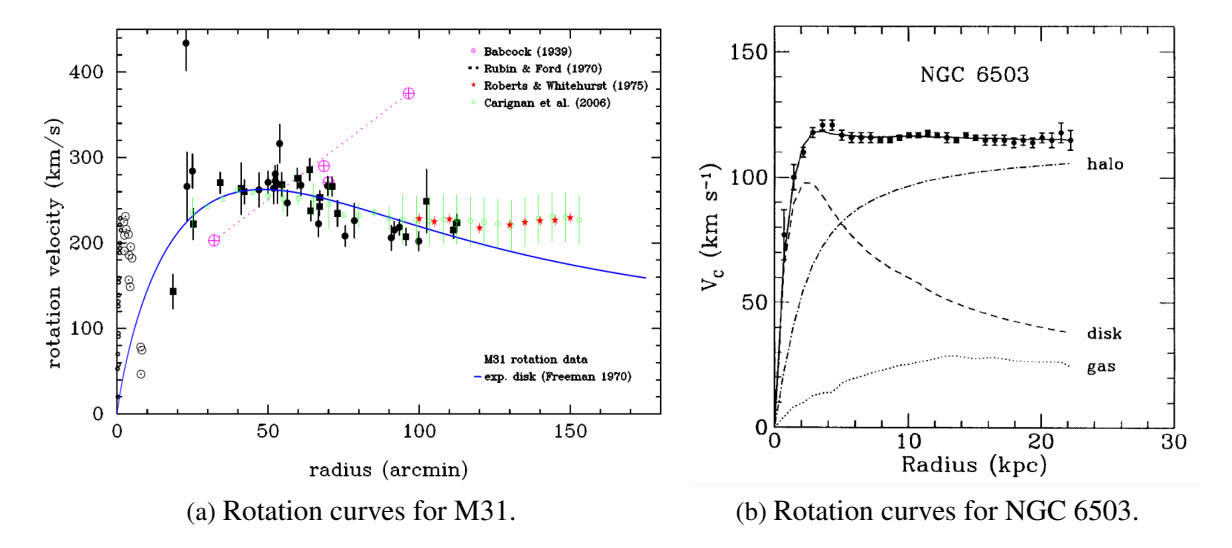


Figure 2.1: Velocity profiles for galaxies a) M31 (observed from 1939 to 2006), and b) NGC 6503 as a function of radial distance from the galactic center. In a) the black solid line corresponds to the rotation curve of an exponential disc with a scale length according to the value given in (Freeman, 1970). The image was retrieved from [BH18]. In b), the image shows the disk and gas contributions plus the dark matter halo contribution needed to match the data. Image retrieved from: [Fre17].

the gas content in a galaxy can be computed as a function of the radio r; it was expected that beyond the stellar disk the rotational velocity decreases as $v \propto r^{-1/2}$. It was not until 1970 when the observations made by Rubin and Ford [RF70] showed a different behaviour, since the velocity seems to flatten for large r, as it can be seen in figure 2.1; this result indicates that there is not observable matter in the outer part of galaxies which increases its rotational velocity. Nowadays, this phenomena is known as $dark\ halos$ with $M(r) \propto r$.

Other observations that supported the existence of dark matter made use of the fact that light bends in the presence of massive objects. In this way, light which comes from a luminous object can be distorted by non visible regions with large mass. An example of strong lensing is shown in figure 2.2, where Tyson et al. used data collected with the Hubble Space Telescope, in it there is a smooth component due to the DM content in clusters in between galaxies [Fre17]. The content of hot gas in clusters also can be explained by DM, since its presence creates the potential well necessary to hold onto the gas. The Chandra x-ray observatory has been studying the Bullet cluster of galaxies, where the content of DM can also be observed with the help of gravitational lensing. These gravitational methods bring evidence of dark matter from scales much larger than those achieved with rotational curves.

All these observations made evident the necessity to include a new type of matter, leading to one of the hardest challenges in modern physics: the search of Dark Matter.

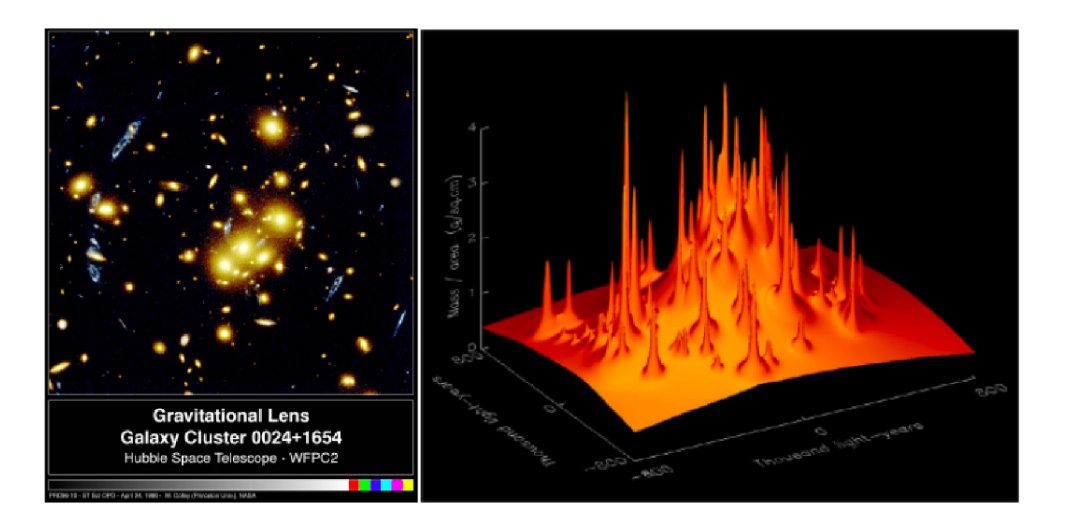


Figure 2.2: Left: The foreground cluster of galaxies gravitationally lenses the blue background galaxy into multiple images. Right: A computer reconstruction of the lens shows a smooth background component not accounted for by the mass of the luminous objects. Retrieved from [Fre17]

2.2 Search of Dark Matter: candidates

With the start of the precision cosmology era it was possible to implement the Λ_{CDM} model, which states that the content of matter in the Universe is 4.9 % ordinary matter (bosons, fermions, hadrons, etc.), 26.3 % dark matter and 68.3 % dark energy [eaPC14]; among these components only ordinary matter is relatively understood. The nature of dark matter is still unknown, although there are models which try to explain it through different schemes such as cosmology, particle physics and modified gravity.

A remarkable fact about the search of DM is that it allows to build a close relation between cosmology and high energy physics. From one side, observations of the power spectrum of the *Cosmic Microwave Background* (CMB) depends on physical measurements: baryon density, dark matter density and dark energy density. On the other hand, the Standard Model (SM) of particle physics is not complete, inasmuch as it is unlikely to explain some properties of the model, DM could bring a solution to these kinds of problems. Based on these results, physicists have come across with Dark Matter candidates, some of them are briefly discussed below.

Dark Matter Particles. By the end of 1980's, DM was thought as a new type of sub-atomic particles:

- Neutrinos: these SM particles used to be thought as DM candidates (*hot dark matter*) due to its lack of electromagnetic and strong interactions, as well as for its stability. Nevertheless, neutrinos as DM particles prevent the formation of large scale structures, excluding them as a suitable solution [BH18].
- Supersymmetry (SUSY): this model was proposed as a solution to the electroweak hierarchy problem and to achieve the gauge coupling unification. SUSY states that

2. Dark Matter

for each fermion in the SM exists a boson with the same quantum numbers (and vice versa), resulting in several numbers of particles known as "super partners". Neutralinos are one of the most studied candidates within this model.

• Axions and Axion Like Particles (ALPs): this particle, an axion, is a Nambu-Goldstone boson which appeared as a consequence of the solution to the *strong-CP problem*. In order to match the observations, the production of axions should have taken place during the early Universe; some of these assumptions make use of the inflationary cosmological model, making this candidate a very interesting one. The mass range of axions is around 10^{-12} eV to 10^{-2} eV (although, an upper bound of 1 eV can be obtain from hot dark matter limits) [Mar17].

The ALPs, as the name suggests, are low mass Cold Dark Matter candidates with properties similar to axions. Although ALPs have not been studied in as much detail as axions [Red19], they could be studied gravitationally in the form of miniclusters. The mass of ALPs m_a have been constrained using galaxy clusters to a mass of around $m_a \leq 10^{-10}$ eV to $m_a \leq 10^{-13}$ eV [Pow16].

• Weakly Interactive Massive Particles (WIMPs): this model proposes the existence of cold non-baryonic particles, which at the same time turn out to be the *relic* dark matter from the early Universe, when the creation and annihilation of dark matter particles and antiparticles was possible thanks to the state of thermal equilibrium. After this epoch, the Universe began to expand and cool, avoiding the creation of DM pairs but allowing its annihilation. As a consequence, the density of DM particles-antiparticles became very low until it reached a constant number, which remains even during the expansion of the Universe. Based on the estimated DM abundance, the cross section of DM pair annihilation is not larger than the cross section for weak interactions.

Classification of WIMPS can be done considering their masses m_χ : low mass candidates have a range of $1~{\rm MeV} \le m_\chi \le 20~{\rm GeV}$, whereas high mass candidates have a mass range of $20~{\rm GeV} \le m_\chi \le 1000~{\rm GeV}$ [Lia16].

• The Dark Photon: this particle is proposed to be a gauge boson which arises from the dark sector of the Standard Model; one of the Dark Matter candidates includes a light vector boson, similar to a dark photon. There are two types of dark photons: the massive kind, which couples to ordinary matter through a current; the massless kind, which does not couple directly to any of the SM currents [FGL20].

Baryonic Dark Matter. Another explanation for the missing matter in galaxies takes into account the presence of compact objects with considerably fewer luminosity than ordinary stars:

• Massive Astrophysical Compact Halo Objects (MACHOs): this proposal takes into

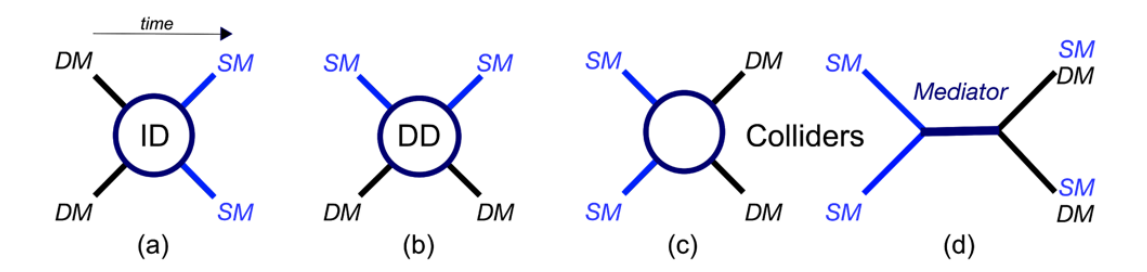


Figure 2.3: Diagram for Dark Matter interactions. a) shows DM annihilation to Standard Model (SM) particles, as sought by Indirect Detection (ID) experiments. (b) shows DM -> SM particle scattering, targeted by Direct Detection (DD) experiments. (c) shows the production of DM particles from the annihilation of SM particles at colliders. (d) again shows the pair production of DM at colliders, but in this case the interaction occurs through a mediator particle between DM and SM particles. Image taken from C. Doglioni & A. Boveia/ATLAS Collaboration [Dog].

account the fact that in the presence of strong gravitational fields, light can be deflected. In this way, gravitational microlensing could be useful to look for compact objects. The MACHO collaboration was aimed to measure microlensing effects in the dark halo of the Milky Way; the results showed that the compact objects do not dominate the missing mass, though.

 Primordial Black Holes: here the exceeding mass consist of black holes created before Big Bang nucleosynthesis. However, the expected number of primordial black holes is negligible compared to the number necessary to achieve the observed effect in rotation curves.

As it can be seen, there are plenty of DM candidates, each of them with specific characteristics which must be taken into account for its detection. The experiments designed, so far, can be classified in three categories: direct detection, indirect detection and search at accelerators ¹

2.2.1 Direct detection

Detection of Dark Matter (DM) particles depends on the type of interaction they can have either with itself or with known particles from the Standard Model. Figure 2.3 summarizes the possible interaction modes with the experimental techniques used to detect them. In the case of direct detection (DD), Dark Mater candidate interacts with a SM particle. The interaction treated in this section corresponds to a scattering process, which is employed at DAMIC and DAMIC-M experiments.

In 1984 Drukier and Stodolsky [DS84] came up with a technique to detect neutrinos through the elastic scattering with nuclei. Some years later, in 1985, Goodman and Witten [GW85] took this same principle in order to detect dark matter particles; three main interac-

¹See more details for latter in the appendix

2. Dark Matter

tion mechanisms were possible: coherent scattering with nuclei (or spin-independent scattering), spin-dependent scattering, and strong interactions. These experiments were thought to be capable of detect nuclear recoil energies of $\sim 1-100$ keV [BH18]. Besides, WIMPs are considered one of the most suitable candidates of DM since, as it was seen before, there is a large number of this particles in the galaxy, making more probable the interaction of a nucleus with DM particles.

Direct detection consists of a DM candidate of mass m_X traveling through a detector, with the possibility of interact elastically with a nucleus of mass m_r . Such interaction could leave a recoil energy as signal in the detector. The differential recoil energy spectrum is given by [Lia16]:

$$\frac{dR}{dE} = \frac{\sigma_0 \rho_0}{\sqrt{\pi} v_0 m_X m_r^2} F^2(E) T(E)$$
(2.1)

Where:

- ρ_0 is the DM candidate density in the local neighbourhood within the galactic halo
- σ_0 is the elastic scattering cross section between the DM candidate and the nuclei. For spin-independent scattering $\sigma_0 \sim A^2 \sigma_{x-p}$, with σ_{x-p} the DM-proton scattering cross section
- m_r is the DM-nuclei reduced mass $m_r = m_X m_T / (m_X + m_T)$
- F(E) is the nuclear form factor
- T(E) is a dimensionless integral over the local DM candidate velocity distribution $f(v_D)$.

Direct detection with nuclei scattering presents a problem, since it has considerable large background from cosmic rays and other sources of interactive radiation particles, therefore detectors have low sensitivity. In order to counteract this issue, detectors are placed underground creating a natural shield for cosmic rays, radiation, etc. Figure 2.4 show the location of underground laboratories until 2017. DAMIC (Dark Matter in CCDs [DAM20]) experiment is part of SNOLAB and, as it will be commented in Chapter 4, has been able to reach high sensitivities; DAMIC-M will be located at Modane Underground Laboratory in France [DM20].

Lately, there has been an effort to study DM candidate with Sub-Gev mass, this is expected to interact with the electron of the atoms instead or through the absorption process. This is a very promising channel for the DAMIC and DAMIC-M experiments [And20], [Blo17].

Among the multiple proposed DM candidates, the number of gravitational and astrophysical experimental searches dominate over the measurements related with the particle nature of DM. For that reason, more collaborations involving different theoretical and experimental



Figure 2.4: Image retrieved from [Fre17]

fields (such as particle, nuclear, condensed matter and atomic physics) are being implemented. Current and future experiments aimed to the search of Dark Matter can be found in the US Cosmic Visions: New Ideas in Dark Matter 2017 Community Report [Mar17].

Chapter 3

Semiconductors

As it was previously stated in the introduction, the present work is based on the DAMIC-M experiment, which is a direct dark matter search detector made of scientific CCDs, more details are provided in the next chapter. Since the basic operation of CCDs is ruled by semi-conductor physics principles, a review of this subject is presented in section 3.1 where silicon semiconductors are considered. The concept of energy bands is presented in order to explain the relation between the conduction of charge of different materials and its band structure. Intrinsic and extrinsic semiconductors are also treated in this section. The use of impure silicon semiconductors enhance the conductivity on the material, allowing better monitoring of the particles interacting with the detector, for this reason silicon doping processes are introduced in section 3.1.1.

The section 3.2 is aimed to enumerate the features of a basic Charged Coupled Device (CCD), considering the case of a three phase device, which is the type of CCD used in DAMIC and DAMIC-M.

For guarantee the most accurate measurements, it is essential to know what defects can affect the performance of semiconductors. The passing of time, defects in its structure and the radiation exposure can affect the quality of the images collected by those experiments that employ such technologies. In section 3.3 the damages which can be found in silicon detectors are presented.

3.1 Silicon Semiconductors as detectors

The use of semiconductors as detectors is based on the interaction of radiation with matter, hence it is necessary to have a material with a high response to energy deposition: the key for choosing a good detector relies on the concept of band structures.

The continuum electronic energy states in a solid formed due to the close proximity of atoms is known as an *energy band*; while a *bandgap* is a region with no available states [Woo18]. As it is known, materials can be classified into three categories according with their facility to conduct charge: conductors, insulators and semiconductors (see more details in the Appendix B.1). These properties are determined by the filling pattern of their energy bands:

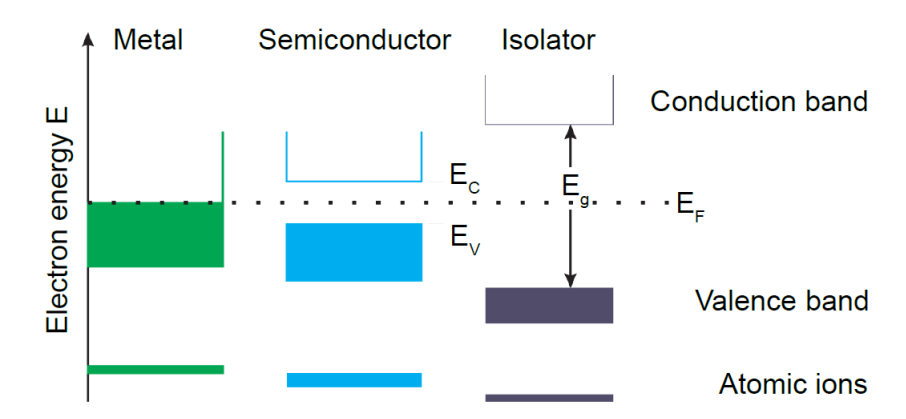


Figure 3.1: Energy bands for three materials: metal, semiconductor and insulator. E_f refers to the energy in the Fermi level. Retrieved from [Jun11].

- valence band: the highest occupied energy band at temperature of zero kelvin [Neu13]. The energy available in this band is denoted by E_V .
- conduction band: the collection of the lowest vacant electronic states [Woo18]. Electrons from this band contribute to the conductivity of the material. The energy available in this band is denoted by E_C .
- bandgap: the gap between the valence band and the conduction band. The energy available in this band is denoted by E_g , this is the width of the forbidden energy band.
- Fermi level: the energy under which all states are filled with electrons and above which all states are empty at T=0 K. Energy in this level is denoted by E_F [Nea12].

As a response to its electron configuration $(1s^22s^22p^63s^23p^2)$, the four valence electrons bonding form a crystal structure. A semiconductor consisting of pure silicon is an intrinsic semiconductor [Spi05], which means that electrons in the conduction band can be generated only by thermal excitation from the valence band, hence the concentration of electrons n in the conduction band is equal to the concentration of holes p in the valence band p. Electrons are fermions, so the probability of occupying a state with energy p is given by the Fermi-Dirac distribution p0, which is function of the temperature p1, the energy in the Fermi level p2 and the Boltzmann constant p3, and the probability for having a vacant hole state p4 are [Spi05]:

$$f_e(E) = \frac{1}{1 + \exp\left(\frac{E - E_F}{kT}\right)}; \quad f_h(E) = 1 - f_e = \frac{1}{1 + \exp\left(\frac{E_F - E}{kT}\right)}$$
 (3.1)

Given the concentration of states in the conduction band N_C and the concentration of

¹Recalling that electrons and holes are two types of charge carriers which contribute to a current

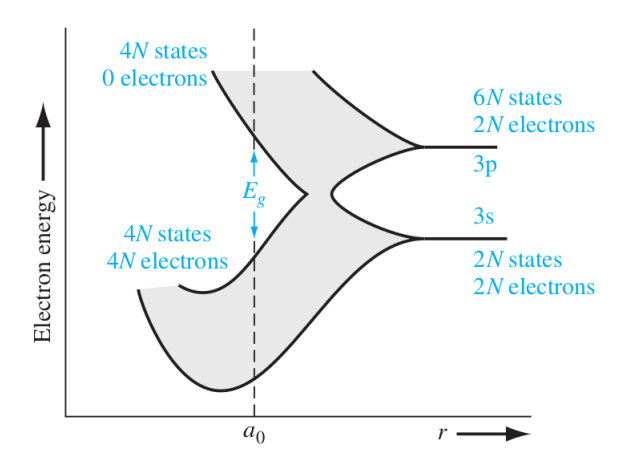


Figure 3.2: Splitting of the 3s and 3p states of Si into the allowed and forbidden energy bands. Retrieved from [Nea12].

states in the valence band N_V , the concentration of electrons and holes is [Neu13]:

$$n = N_C \exp\left(-\frac{E_c - E_F}{kT}\right); \quad p = N_V \exp\left(-\frac{E_F - E_v}{kT}\right)$$
 (3.2)

Since the concentrations of electrons and holes are the same $n_i = n = p$, the energy in the Fermi level is in the middle of the bangap, the intrinsic level $E_F = E_g/2$. The resulting intrinsic charge carrier concentration is:

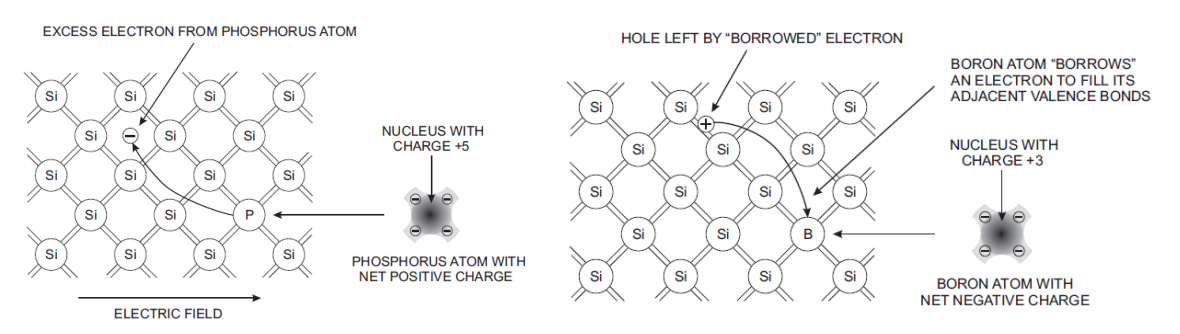
$$n_i^2 = np = N_C N_V \exp\left(-\frac{E_g}{kT}\right) \tag{3.3}$$

With $E_g = E_C - E_V = 1.12$ eV at T = 300 K [Neu13]. Besides, the energy required for generating a pair electron-hole is 3.62 eV at the same temperature [LR12].

Figure 3.2 shows the band splitting of Si. 3s and 3p states overlap as the interatomic distance decreases, and at the equilibrium distance a_0 it splits again forming 4 quantum states per atom in the lower band and 4 quantum states per atom in the upper band. The lowest band corresponds to the valence band, while the upper band is the conduction band. The energy of the bandgap E_g is the width of the forbidden energy band [Nea12].

3.1.1 Silicon doping

Pure Si have a low concentration of charge carries, since the band gap of around $E_g=1.12$ eV is larger in comparison to kT=0.025 eV at T=300 K (as a large bandgap corresponds to an insulator). In order to use Si as a detector, the conductivity has to be modified, this can be done with the addition of a *dopant* which helps to increase the concentration of free charge carriers. Doping can be done replacing a Si atom with another one from an element belonging to either the XIII (B, Al, Ga, etc.) or XV (N, P, As, etc.) groups of the periodic table, in this way Si becomes an n-type or p-type materials [Spi05], [Jun11]:



- (a) Si lattice dopped with phosphorus
- (b) Si lattice dopped with boron

Figure 3.3: Schematic view of the two-dimensional Si lattice a) dopped with phosphorus (n-type doping introduces a lightly bound electron that can move freely under the influence of an electric field), b) dopped with boron (p-type doping leaves an unpaired silicon bond which can attract a neighbouring electron, the resulting vacancy -a hole- moves through the lattice). Retrieved from [Spi05].

- n-type: in the addition of one atom containing five electrons of valence (for example, phosphorus), four of them attach to the Si atoms via covalent bond and the remaining electron is weakly bound and it is promoted to the conduction band at room temperature. Phosphorus is left as positively charged, i.e, in a donor state where electrons are the free charge carriers (figure 3.3a).
- p-type: if the dopant element has three electrons in its valence shell (such like boron), one electron is missing to complete the bounding with Si, hence a hole is created in the valence band. Boron is left as negatively charged, namely in an acceptor state where holes are the free charge carriers (figure 3.3b).

Once Si has been n- or p-dopped, the semiconductor is said to be *extrinsic*, now it can have a predominance of either electrons (n-type) or holes (p-type) introducing new levels in the bangap. The concentration of electrons occupying the donor state n_d , and the concentration of holes p_a occupying an acceptor state are [Nea12]:

$$n_d = \frac{N_d}{1 + \frac{1}{2} \exp\left(\frac{E_d - E_F}{kT}\right)} \tag{3.4}$$

$$n_d = \frac{N_d}{1 + \frac{1}{2} \exp\left(\frac{E_d - E_F}{kT}\right)}$$

$$p_a = \frac{N_a}{1 + \frac{1}{4} \exp\left(\frac{E_F - E_a}{kT}\right)}$$
(3.4)

In equation 3.4 n_d is the density of electrons occupying the donor level and E_d is the energy of the donor level, the factor 1/2 is related to the spin factor. In a similar way, in equation 3.5, N_a is the concentration of acceptor per atom, E_a is the acceptor energy level, and the factor 1/4 is associated with the acceptor level in Si.

3. Semiconductors

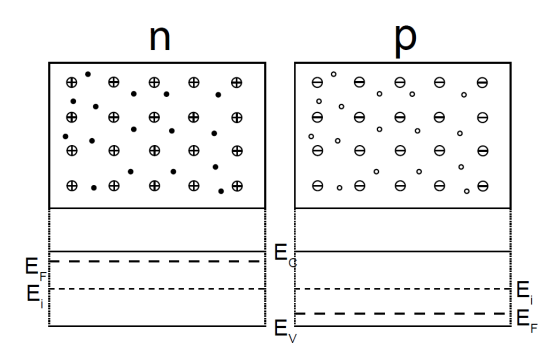


Figure 3.4: P-n junction before contact. Electrons are represented by filled circles; holes, by empty circles. Retrieved from [Jun11].

3.1.2 Silicon Diode

A large number of semiconductors contain a junction of both n-type and p-type semiconductors [Nea12], the interface between these two dopped regions is called the *pn junction*. Before joining together, the p- and n-type silicon are electrically neutral; figure 3.4 shows both semiconductors with their respective band diagrams, the p-side has an excess of holes (empty circles), the n-side has an excess of electrons (filled circles), E_F is the energy in the Fermi level, while E_i is the energy for the intrinsic Fermi level and it is located in the middle of the bandgap [Jun11].

The junction is in thermal equilibrium when no voltage is applied, hence the Fermi level energy remains constant through the system. Once both regions are in contact, thermal diffusion will drive holes and electrons across the junction. Under thermal equilibrium electrons from the n-region will diffuse into the p-region, leaving positively charged donors behind. In the same way, holes will diffuse from the p-region into the n-region, this time negatively charged acceptor atoms are exposed. The net positive and negative charges in the n- and p-regions, respectively, induce and electric field from the positive to the negative regions [Nea12].

The figure 3.5a shows the diffusion of electrons and holes. The figure 3.5b is a scheme of the band structure for the pn junction, it can be seen how the energy in the intrinsic Fermi level changes between p and n regions, hence the conduction and valence bands also bends during this transition in order to maintain a constant Fermi level. This potential distribution creates a *built in potential* V_{bi} between the p- and n- regions [Spi05].

The diffusion of electrons and holes have as consequence the creation of a region free of mobile carriers, this region is called the *depletion region*. All electrons and holes are swept out from this region due to the electric field [Spi05].

If an external electric field is applied, thermal equilibrium is broken. Such voltage can be positive [Spi05]:

• Forward bias: a positive potential is applied to the p-region and a negative one to the

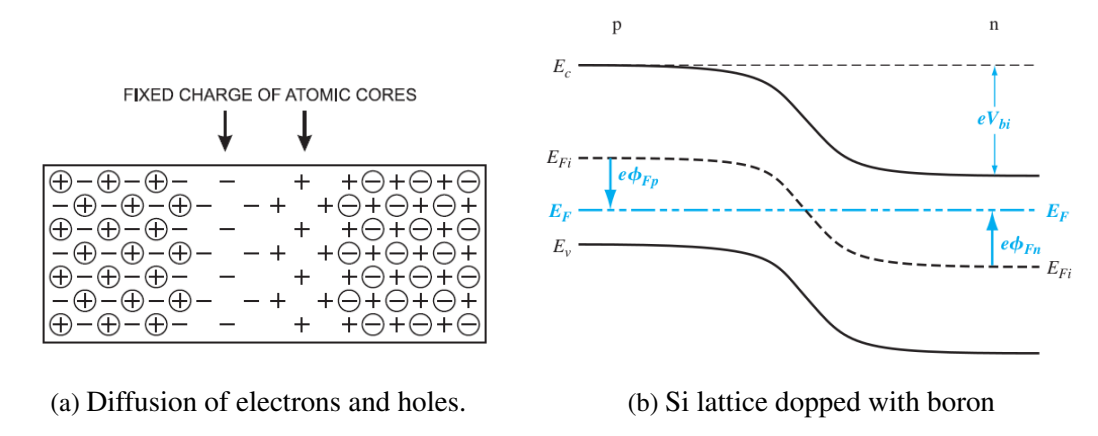


Figure 3.5: a) The diffusion of electrons and holes across the p-n junction forms a depletion zone with a resulting potential between the p- and n-regions. Retrieved from [Spi05]. b)

n-region, hence the potential barrier is reduced increasing the flow of electrons and holes through the junction.

- Reverse bias: a negative potential is applied to the p-region and a positive one to the
 n-region, hence the potential barrier is increased, thus the width of the depletion region
 increases. The leakage current of diode is the current that the diode will leak when a
 reverse voltage is applied to it
- Flat band: When any bias voltage is applied, the band structure is held without deformations.

The depletion region forms a capacitor, due to the lack of mobile carriers. In this case, the depletion regions are the dielectric and the undepleted p, n-regions are the electrodes [Spi05]. Radiation detectors use reverse biased diodes with an external potential V_b , where the potential V in the depletion region changes perpendicularly to the n-p interface. Besides, the mobility μ of electrons is approximately three times the mobility of holes: $\mu_e \approx 3\mu_h$.

A highly important function of a semiconductor detector is the charge collection. The transport of carriers can be done through:

- Diffusion: carriers move in random directions due to the thermal energy present, the
 net motion has a direction in the opposite direction of higher concentrations. The
 concentration of carriers has a Gaussian distribution given by the diffusion constant D
 which depends on the material employed.
- Drift: carriers are moved by the presence of an electric field. The velocity of the carriers is given by: $\vec{v} = \mu \vec{E}$

Once the detector interacts with radiation, mobile electrons and holes are created and moved by the presence of an electric field. Electrons and holes move in the opposite direction, contributing to the signal current. The *collection time* is defined as the time a carrier

3. Semiconductors

needs to move throughout the sensitive volume.

Both the doping impurities present in semiconductors and defects originated from the growing of silicon wafers can contribute to current measurements during the detection process, this issue can lead to misinterpretations of the data acquired, hence it is essential to understand the origin and behaviour of such defects in order to improve the precision of semi-conductor detector experiments. Before listing some of the main defects, the basic structure of a three phase silicon Charged Coupled Device is presented in the following section

3.2 Charged Coupled Devices as Silicon semiconductors

The Charge Coupled Device (CCD) was invented by Willard S. Boyle and George E. Smith at Bell Telephone Laboratories in October 19, 1969 [Jan01]. Originally, the CCD was thought to work as a memory device, however its use as an imaging detector resulted in a better application (for its advantage in size, weight, ultra low noise, dynamic range, reliability and durability).

In CCDs a *bit* of information is made up by a packet of charges [Jan01] (electrons or holes) which are stored in a depletion region of a metal-oxide semiconductor (MOS) capacitor. The charges are moved across the CCD circuit by placing MOS capacitors very close to each other and manipulating the voltages on the gates of the capacitor in such a way that the charge spills from one capacitor to the next. The charge packet is then detected by an amplifier providing an output voltage.

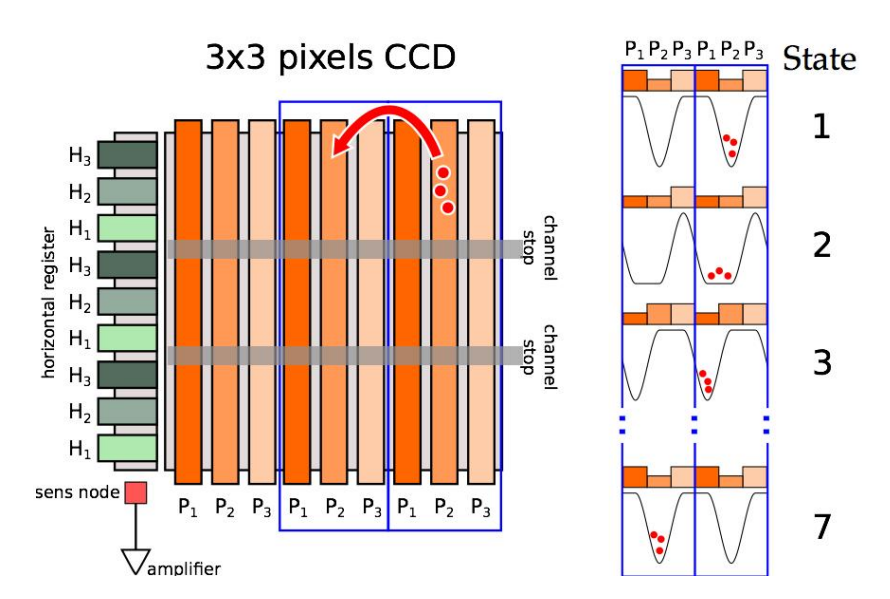


Figure 3.6: Three-phase CCD. Retrieved from [Lia16]. Image by Javier Tiffenberg.

The simplest arrangement for a CCD is a three-phase device, wherein the gates are placed in parallel with every third gate connected to the same clock driver. One pixel is formed by three of these gates, which in turn make up a pixel register when connecting to the phase-1, -2 and -3 clocks.

This cycle is applied repeatedly until the charge arrives to the horizontal register, where it is moved vertically modifying the relative voltages H_1 , H_2 , H_3 in the same way as with P; when the charge arrives to the last horizontal node, it is read out by an amplifier where the charge contained in each pixel is transformed into a voltage. The vertical registers are divided by channel stops, which are potential barriers that avoid the spread of the signal charge from one column to the other.

In a CCD the primary performance functions for generating an image are [Jan01]:

- 1. Charge generation: this is the ability to intercept an incoming photon and generate an electric charge. The fraction of incident photons that produces a useful charge is known as *Quantum Efficiency*. This quantity depends on the wavelength of the incoming photon, which interacts with the detector only if it is higher than the bandgap (in the case of silicon, higher than 1.12 eV).
- 2. Charge collection: refers to the ability to accurately reproduce an image from the electrons generated.
- 3. Charge transfer: during this stage, the charge is moved by manipulating the voltage in the device
- 4. Charge measurement: here, the detection and measurement of the charge collected in each pixel is done by dumping the charge onto a capacitor connected to an output amplifier.

3.3 Damage in Silicon semiconductors

Damage in the silicon lattice is not only a consequence of growing techniques, it is also a common problem when semiconductors are placed in an environment with high energetic radiation, such as those operated at colliders or in space. For instance, tracking detectors at LHC are located close to the interaction point where the harsh radiation causes displacement damage which affects the properties of the sensor; in the case of space radiation, detectors face the flux of highly energetic particles, reducing the lifetime of the devices.

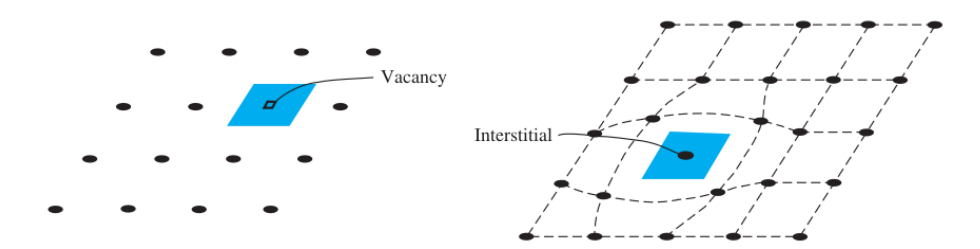


Figure 3.7: Schematic view of a single-crystal lattice showing in the left side a vacancy defect; the right side shows an interstitial defect. Retrieved from [Nea12].

3.3.1 Crystal defects

A real crystal can have defects due to its geometrical composition, the finite array of silicon atoms creates an incomplete bond among them. These defects can be classified into four categories: point defects, line defects, area defects and volume defects [Sze12].

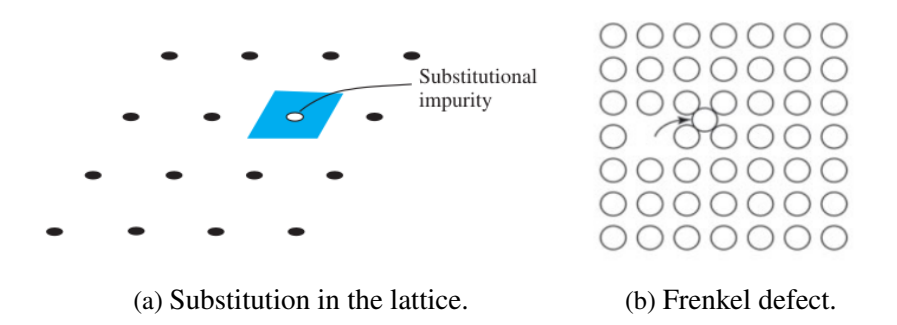


Figure 3.8: Two-dimensional representation of a) a foreign atom substituting a silicon atom in the semiconductor lattice. Retrieved from [Nea12]. b) Frenkel defect. A host atom is located between lattice sites and near a vacancy. Retrieved from [Sze12].

A *point defect* is the result of a missing atom in the lattice, it creates a *vacancy*. The opposite situation occurs when a foreign atom is located between lattice sides, in this case the effect is known as an *interstitial defect*; this foreign atom can also completely substitute the site of a silicon atom in the array [Nea12], [Sze12]. Figure 3.7 shows a representation of the vacancy and the interstitial defects, whereas in figure 3.8a the substitution of a silicon atom is shown. It is possible to have a contribution from both vacancy and interstitial defects due to their close proximity, this effect is known as a *Frenkel defect*, as it can be seen in figure 3.8b. Vacancy and interstitial defects change the geometrical array of the crystal and interferes with the chemical bonding between silicon atoms, as well.

Line defects occur when a lineal array of atoms is inserted into the lattice. This effect is also called a dislocation; there are two types of dislocation: edge type and screw type. In the first type, edge dislocation, an extra plane of atoms AB is inserted into the lattice, as it can be observed in figure 3.9a. Screw dislocation, figure 3.9b, occurs when the crystal is divided creating a space in the lattice.

The atomic thermal vibration of the silicon atoms in the lattice is the origin of another type of defects, such atoms have thermal energy which is a function of the temperature. Lattice vibrations are the defects generated by the random thermal motion of the space between each atom because of thermal vibration. [Nea12].

3.3.2 Radiation damage

The damage in the semiconductor lattice can also be a consequence of the exposure of silicon detectors to environments with high levels of radiation. Radiation damage can be transient (which is associated with secondary effects generated by ionization effects [van63])

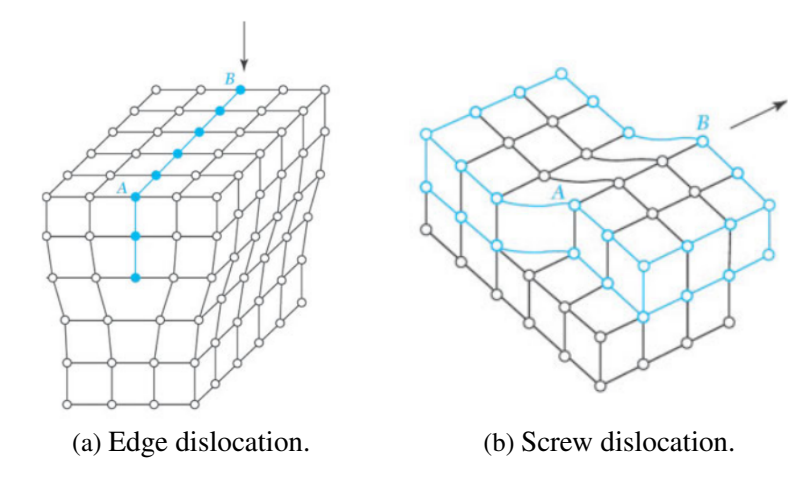


Figure 3.9: Schematic view of line defects: a) edge dislocation and b) screw dislocations. Retrieved from [Sze12].

or permanent (which lead to a irreversible degradation of the detector, reducing its effective lifetime) [Woo18]. Permanent defects are, in turn, classified in two more categories: surface damage and bulk damage.

Surface damage

As it was mentioned in section 3.1.1, electrons have higher mobility than holes which makes it possible for holes to get trapped in oxide traps close to the silicon-silicon oxide boundary inducing a threshold-voltage shift which depends on the oxide layer thickness [Woo18].

Bulk damage

In this case, particles passing through the semiconductor may collide with the lattice giving part, or all, of its energy to a silicon atom inducing defects in the detector such as vacancies, interstitials or Frenkel pairs.

When a particle has a considerable amount of energy, it can transfer kinetic energy to an atom in the lattice in the form of recoil energy E_r through either elastic or inelastic collisions; the initially displaced atom is also known as the *primary knock-on atom* (PKA) and, in order to obtain this first displacement it is necessary that the imparted energy is higher than the displacement threshold energy [Mol99] (which is around 25 eV for silicon [Woo18]).

The PKA recoil energy can be employed to displace further atoms or ionize them creating, initially, single or point defects to end with interstitial defects [Jun11], and consequently, loosing such PKA energy.

3.3.3 Characterisation of damage in semiconductors

The defects described above affect the performance of the detector, fortunately there are techniques which are used to treat such damage in order to measure and correct it.

Trap-pumping

This process involves the alteration of the clock phase in such a way the signal packet is pumped (i.e., moved backwards and forwards) between two adjacent pixels N times. As consequence, the effect created by any considerable charge captured within the pixels can be amplified [Woo18].

The trap-pumping method presents some limitations in its usage [Woo18], for instance only allows probing for defects which are electrically active and are able to capture signal charge carriers. Besides, if the defects are not detected by trap-pumping, the charge transferred does not affect the image quality.

Deep Level Transient Spectroscopy (DLTS)

This technique allows for the study the properties of defects located in the depletion regions of the semiconductor. A variety of traps in the semiconductor can be detected using a high frequency capacitance thermal scanning method [Lan74].

DLTS works as follows [Woo18]: on a diode that is connected in reverse bias, a voltage pulse is applied allowing free carriers to move across and re-charge the defects that are present. When the pulse has passed, the defects will emit via thermal emission. Since the diode is storing charge for a finite time within defect states, when the defect charges are recovered, a transient capacitance in the depletion region is generated.

3.3.4 Sources of noise in CCDs: Dark Current

During the different operation stages of a CCD, there are sources of noise which can affect the sensitivity and image quality of the devices. Among the different sources of noise, the *Dark Current* (DC) is treated in this work since the charge from a signal and from DC are collected in the same way [Woo18], hence it is important to implement a method to reduce the level of this noise in the CCDs at DAMIC and DAMIC-M experiments for having more sensitive detectors.

The Dark Current arises during charge generation [Woo18], it is intrinsic to semiconductors and is caused by the thermal generation of minority carriers [Jan01]. The three main regions where DC can be generated are [Jan01]: neutral bulk material below the potential well and channel stop regions, depleted material within the potential well and Si-Si₂ interfaces states. Figure 3.10 shows a schematic view of the different regions that contribute to DC, being the surface of the semiconductor where the higher amount of DC is found due to the presence of interface traps [Woo18]. Consequently, the there are three main sources of

DC in a CCD related with such regions [WBW⁺02]:

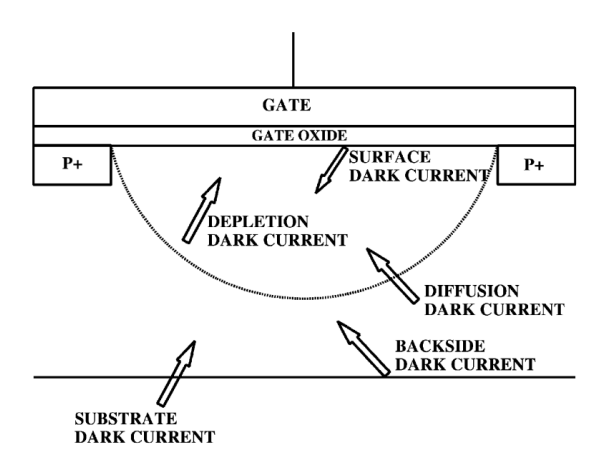


Figure 3.10: Schematic view of the three main regions that contribute to the Dark Current generation. Retrieved from [Jan01].

• Depletion or bulk DC: as the name indicates, this contribution is generated in the depletion region of the CCD where the concentrations of electrons n and holes p are lower than the intrinsic concentration n_i $(n, p << n_i)$.

The Dark Current in electrons per pixel per second De_{dep}^- is given by [WBW⁺02]:

$$De_{dep}^{-} = \frac{x_{dep}A_{pix}n_i}{2\tau} \tag{3.6}$$

Where A_{pix} is the area of the pixel, τ is the carrier lifetime; x_{dep} is the width of the depletion region and n_i is the intrinsic carrier concentration.

- Diffusion DC: this contribution arises when a part of the CCD remains field-free.
- Surface DC: such type of DC is generated in the interface of the Si-Si₂.

It is known that DC increases linearly with temperature [Woo18], [Jan01], hence its effects can be considerably reduced by cooling the CCD. Figure 3.11 shows the logarithm of the DC in a CCD vs the inverse of the temperature computed by [WBW+02]; the left side of the image corresponds to a single pixel, whereas the right side shows the evolution corresponding to four random pixels.

According with some results obtained by the company EEV, which supplied the European Southern Observatory (ESO) with CCD called EEV44-82, the dark current is a function of the temperature. The CCD was cooled to reach -95° C (178K) to achieve a low level of noise of $10e^{-}$ /pix/hour [Cav]. In the figure 3.12 how the theoretical dark current differs from that measured, the level of DC is slightly higher than expected (this fact is similar to the results found with the DAMIC CCDs, which we tried to reproduce in this work and tried to explain why).

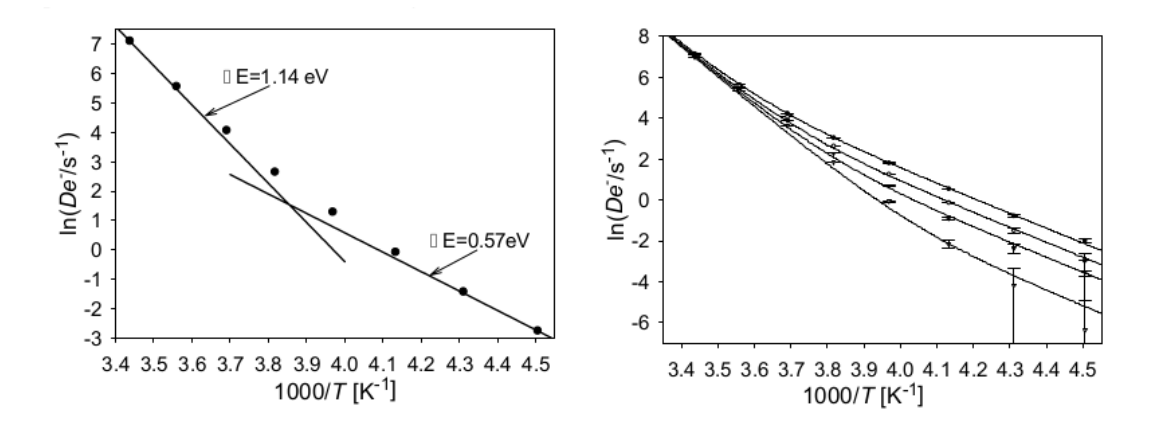


Figure 3.11: *Left:* Average of the logarithm of the dark current vs. the inverse temperature. *Right:* The logarithm of the dark current vs. the inverse temperature for four random pixels. The fits are based on the model assuming different impurity concentrations. Retrieved from [WBW⁺02].

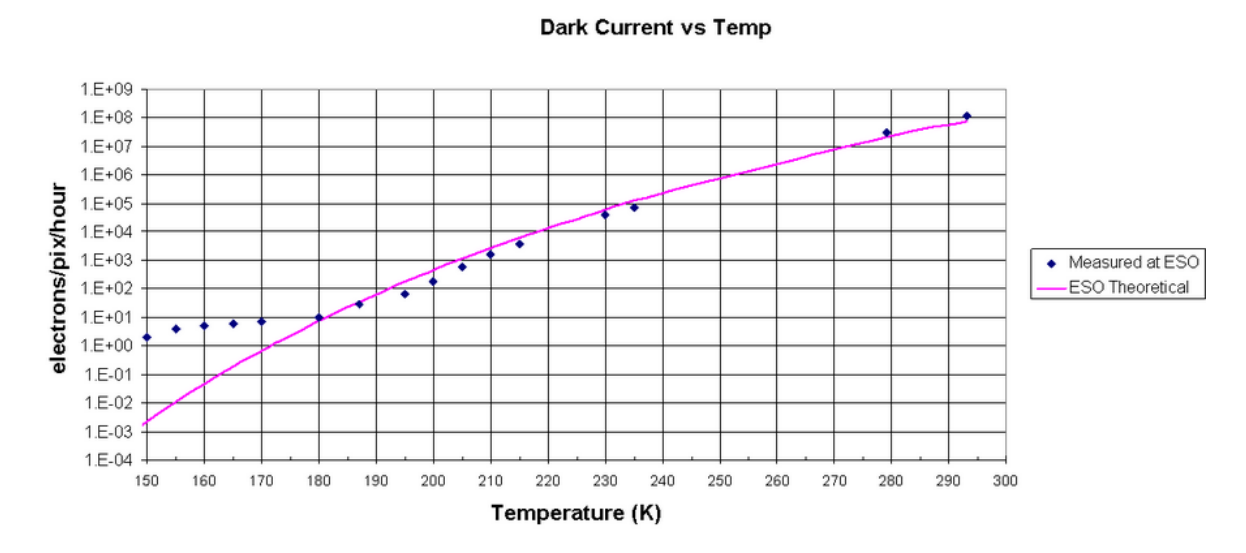


Figure 3.12: Schematic view of the three main regions that contribute to the Dark Current generation. Retrieved from [Cav].

Chapter 4

DAMIC and DAMIC-M

DAMIC (DArk Matter In CCDs) is an experiment designed for the direct detection of DM particles which interact with the nuclei and electrons in the silicon bulk of a fully depleted scientific-grade CCD [Set20]. Due to its low noise and low dark current, the CCDs employed are sensitive to WIMPS with masses in a range of $1 - 10 \text{ GeV}/c^2$.

DAMIC is installed at SNOLAB, an underground laboratory located 2 km below the Creighton Mine in Ontario, Canada [SNO06]. During the period of 2013-2020 a R&D program was carried out with the aim of test the potential of the experiment [DAM20]:

- The nuclear recoil energy scale was calibrated with a CCD and a low-energy photoneutron source [CTAA⁺14]
- Measurements of the background contamination were provided [AAAB⁺16]
- A low-mass WIMP interacting with electrons search with 11 kg-day of data was performed to prove the stable, low-noise and low-background of a CCD array located in an underground laboratory [AAAB⁺20].

Currently, a DAMIC detector of 40 g has been collecting data for calibration, radioactivity studies and for DM searches [Set20].

In this chapter the experimental setup for DAMIC and DAMIC-M and its detection technique are described very briefly, putting emphasis on the use of CCD as a DM particle detector. For more details see [DM20] and references in this work. The current status of the damage study in CCDs along with its characterisation is also discussed.

4.1 Experimental setup

The bulk of the CCDs, which has a thickness of 675 μ m, can detect coherent elastic scattering of WIMPs. A single CCD has an area of (6×6) cm², a mass of 5.9 g and a resolution of 16 Mpixels, with a pixel size of $(15 \times 15) \mu$ m² [Set20]. Each CCD is attached to both a silicon backing and a flex cable which provides the voltage biases, clocks and video signals necessary for drive and reading of the device; then, these components are packaged together in a copper module, see figure 4.1. These modules, in turn, are inserted in slots of a copper box; the current array at SNOLAB consist of seven modules, giving a mass of 40 g

(figure 4.2).

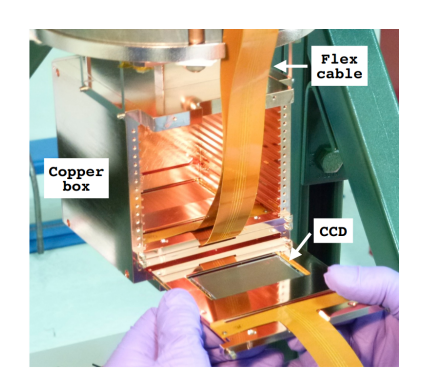


Figure 4.1: Low-radioactivity copper module holding a CCD. The flex cables carry the CCD signals. Retrieved from [AAAB⁺16].

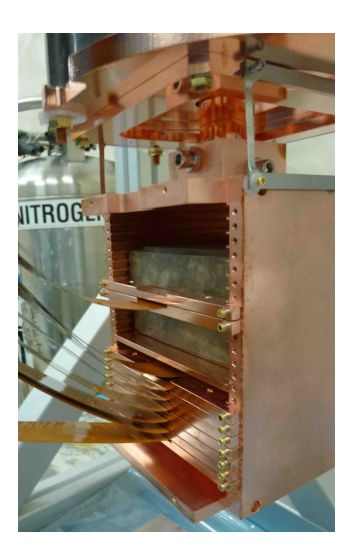


Figure 4.2: Current DAMIC array at SNO-LAB consisting of seven CCDs for a total mass of 40 g. Retrieved from [Set20].

In order to attenuate the possible noise sources, the copper box is cooled to ~ 140 K inside a vacuum chamber and shielded on all sides as follows: a 18 cm of lead is suspended above the box inside the vacuum vessel, with the innermost 2-inches made of lead from an ancient Spanish galleon which suppress the background from bremsstrahlung gamma rays produced by decays in the outer lead shield; this final shield consists of 42 cm-thick polyethylene to moderate and absorb environmental neutrons. A schematic view of the shielding is presented in figure 4.3. The overburden of the laboratory site strongly reduces the cosmic muon flux to a rate of $< 0.27 \text{m}^{-2} \text{d}^{-1}$ [AAAB⁺16].

Besides the strong shielding, due to the features of the CCDs, DAMIC has a high spatial resolution as well as an exceptional energy response, which is helpful for identifying and suppressing radioactive background [CM20]. With an exposure of 3×10^4 - 10^5 s (about 8 and 24 hours), one image is acquired, then a zero-length ("blank") exposure is taken for noise and detector monitoring. From all data recorded, up to December 2018, a total of 7.6 kg day exposure has been recorded for background studies and data characterisation, while around 13 kg day exposure data are used for DM searches [Set20].

The CCDs feauture a three-phase polysilicon gate structure (see section 3.2) with a buried p channel (figure 4.4a), while the bulk of the CCD is made of n-type silicon with a high resistivity ($10 - 20 \mathrm{k}\Omega\mathrm{cm}$), allowing for a low donor density in the substrate ($\sim 10^{11}\mathrm{cm}^{-3}$). Hence, the bias voltage needed for a fully depleted operation is low as well ($\sim 20\mathrm{V}$).

Direct detection of WIMPs at DAMIC considers a particle of DM scattering off either the silicon nuclei or electrons. Since the CCD is operated at full depletion, the ionization charges are drifted along the direction of the electric field (z axis) and collected on the pixel array (xy plane) as it is represented in figure 4.4b. Besides, the charge carries (holes)

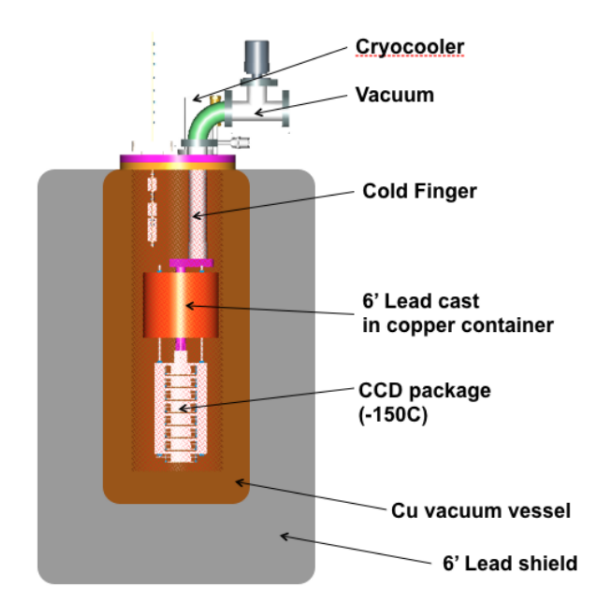


Figure 4.3: Schematic of DAMIC vacuum vessel and shield. Retrieved from [BCD⁺12].

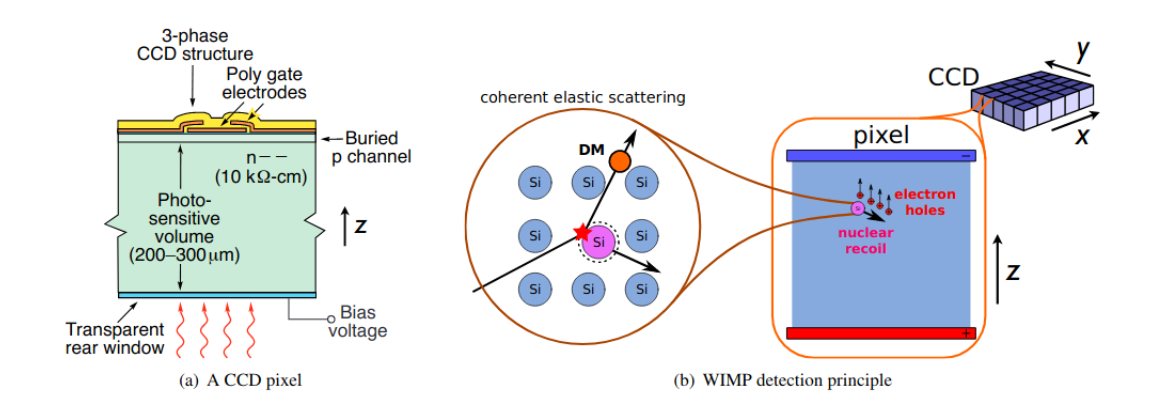


Figure 4.4: a) Cross sectional diagram of a $(15 \times 15) \mu \text{m}^2$ pixel in a fully depleted, back illuminated CCD. b) Representation of the WIMP-nucleon scattering, where the scattering of a DM particle with a Si nucleus leads to ionization being produced in the bulk silicon. The charge carriers are then drifted along the z direction and collected at the CCD gates. Retrieved from [CTAA+14]

will be collected and held near the p-n junction, a few μ m below the gates. Due to thermal motion, the charge diffuses transversely with respect to the electric field direction as it is drifted, with a spatial variance ($\sigma_x^2 = \sigma_y^2 = \sigma_{xy}^2$) proportional to the transit time ¹ (see figure 4.5). Charges produced by interactions closer to the back of the CCD will have longer transit times, which result in greater lateral diffusion.

Figure 4.5 also illustrates how the maximum observed lateral spread ($\sim 20 \mu m$) occurs for ionization events on the back surface of the device for which ~ 25 pixels collect 95% of the generated charge carriers [AAAB⁺16]. There is a positive correlation between the lateral diffusion of the collected charge on the pixel array σ_{xy} and the depth of the interaction z (i.e., $\sigma_{xy} \propto z$), which allows to make a three-dimensional reconstruction of the position of

¹depth of the interaction point

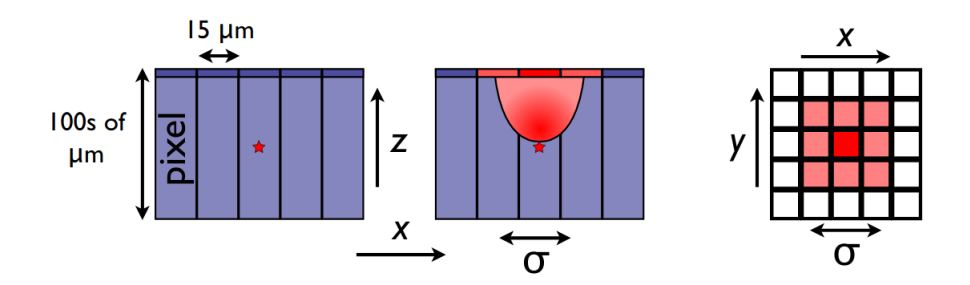


Figure 4.5: Depiction of a point-like particle (star) interaction within the CCD bulk. The charge is drifted along the z axis and it diffuses as it travels toward the gates. This leads to a spatial distribution of the charge on the xy plane whose variance (σ_{xy}^2) is proportional to the charge transit time. From this lateral spread it is possible to reconstruct the depth of the interaction. Retrieved from [CTAA⁺14].

the energy deposit in the bulk of the device, along with the identification of particle types based on the cluster pattern (figure 4.6b). The calibration of the diffusion parameters is carried though the tracks of traversing muons and X-ray events interact near the surfaces on the back and the front of the CCD [Set20].

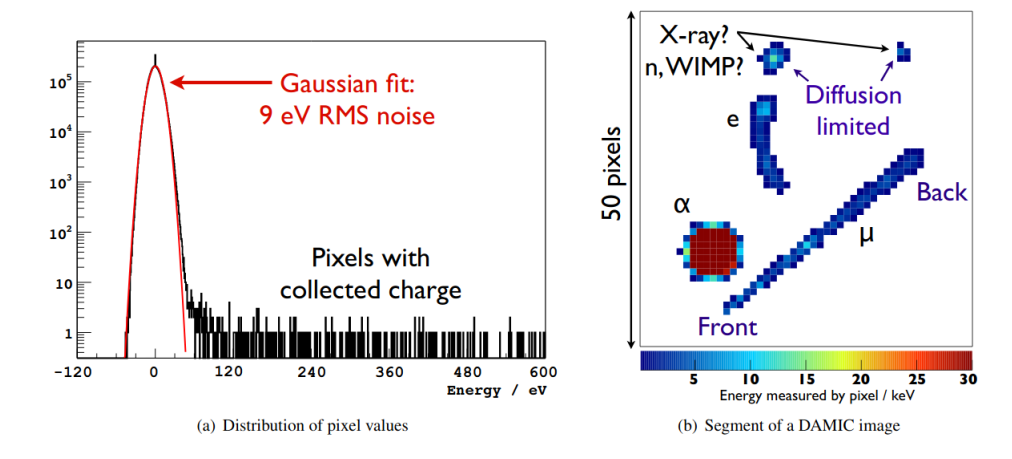


Figure 4.6: a) Pixel value distribution for an image after the median pixel value over many images has been subtracted. Readout noise is the Gaussian distribution, while the right side tail corresponds to pixels where charge has been collected . b) Image reconstructed from a measured 50x50 pixel exposed to a ²⁵²Cf source on the surface. Clusters from different types of particles can be observed Retrieved from [CTAA+14].

The collected charge is held at the gates during hour-today-long image exposure, until the readout is performed. The readout consists of the transfer of the charge from one pixel to the next one in y direction along each column through "parallel clocks", see Appendix C for more details. The inefficiency of the charge transfer is low (10^{-6}) , the readout noise for the charge collected in a pixel is $\sim 2e^-$ [AAAB⁺16].

The number of dark electrons, i.e. electrons produced by thermal excitation in the Silicon substrate, collected is proportional to the exposure time, and produces a Poissonian noise. The calibrations to select the pixels with significant charge were done by illuminating the the CCD with x rays from known sources (like oxygen, aluminium, silicon, and others),

having as a result a linear dependence between the CCD output and low energy signals [AAAB⁺16].

The search of rare events requires the longest possible exposures, in the case of DAMIC, the small amount of dark current of the CCDs ($< 10^{-3}e^{-}\mathrm{pix}^{-1}\mathrm{day}^{-1}$ at $\sim 120\mathrm{k}$) allows the exposure of several days without adding noise [AAAB⁺16]. Up to 2018, DAMIC has collected about 7.6 kg day exposure for background studies and calibration, and around 13 kg day exposure for Dark Matter search. The charges for calibration and background are collected by each pixel, and read out individually to maximize spatial resolution (this is known as 1x1 readout configuration). On the other hand, charges in the second data set are collected and transferred by column segments of 100 pixels into the serial register before the charge is clocked in the x direction, then each column segment is read out individually (1x100 readout configuration). CCDs are read with an integration time for the correlated double sampling of 40 μ s, leading to an image readout time of either 849 s in 1x1 or 20s for 1x100 configurations.

4.1.1 DAMIC-M

A new collaboration is working on a heavier version of DAMIC, which will allow for a detector with better sensitivity. *DAMIC at Modane* (DAMIC-M) will be located at the Modane underground laboratory (LSM) in France, with the following features [Set20], [DM20], [CM20]:

- CCDs consist of 6k ×6k pixels over a (9 × 9)cm² area and a thickness of 1mm, for 20g of mass. A one-kg detector will have 50 CCDs increasing the target area mass.
- Skipper-CCD technology capable of achieving sub-electron resolution on the signal measurements.
- the background level will be reduced to a fraction of dru, i.e., the background level $(1dru \sim 1 \text{ event keV}^{-1}kg^{-1}day^{-1})$.

The new readout system, or "skipper amplifier", implements floating gate for the output channel, allowing charges to "skip" past output contact [JL20]. In this way, the pixel charges are sampled multiple times before being readout, which translates into a high-resolution detection of a single electron and a higher sensitivity, since only few eV energies could release an electron in silicon. This resolution in addition with the low leakage current will make possible to acquire a threshold down to $2 \sim 3$ electrons.

Figure 4.7 left, shows a sketch of the DAMIC-M array. The right side of this figure presents the high-resolution detection of a single electron's response to the skipper amplifier with a 675μ m-thick 6 Mpixel CCD, achieving a readout noise of $0.07e^-$ with 4000 samples per pixel [TSHDW⁺17].

The DAMIC-M experiment is still in progress, readout electronics and detector system are

4. DAMIC AND DAMIC-M

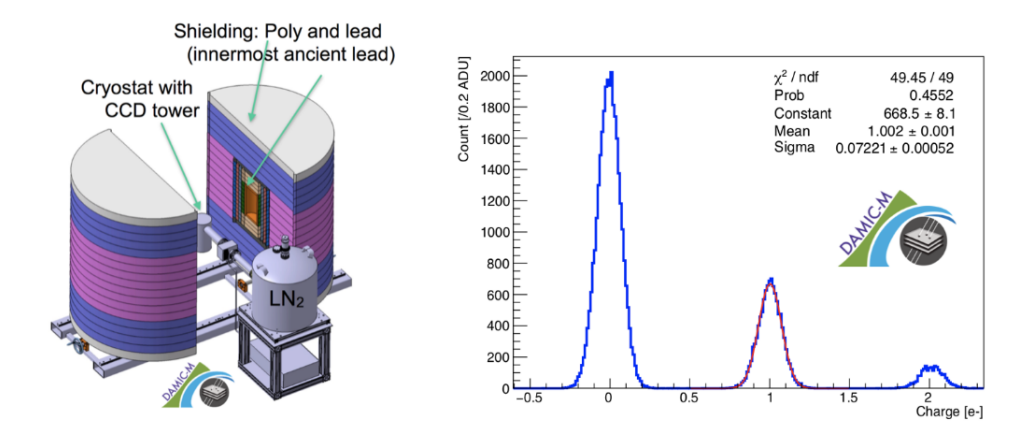


Figure 4.7: Left: sketch of the DAMIC-M design. Right: single electron resolution measured on a prototype of DAMIC-M skipper-CCDs (with 1000×6000 pixels and 675μ m thickness). Retrieved from [Set20].

being developed, (mainly with the purpose of reducing the background); during the second half of 2023 the detector will be tested in a clean-room environment at LSM.

As it was mentioned in Section 3.3.4, the dark current (DC) is an important source of noise in CCDs, hence it is necessary to study the level of DC in order to know the level of noise in the experimental array and to understand the type of the present defects and its origin as well. This is the subject of the following chapter.

Chapter 5

Data analysis of the dark current

In this chapter, the actual test-stand CCDs at the Institute of Physics of Cantabria (IFCA by its Spanish initials) is presented. The original idea of this work was to prepare the laboratory system in order to take some measurements of the dark current in the CCDs. Unfortunately, due to the health emergency caused by the Covid-19 pandemic, it was infeasible to acquire the equipment and assemble the CCD setup during the Master course 2019-2021.

In view of the facts, data from DAMIC, collected in 2017 and 2019, is analysed instead. This analysis is made in order to understand how it has to be treated and to know the level of dark current present in the CCDs.

5.1 Test-stand CCDs at IFCA

The system that will be used is one similar to the system employed by the Nuclear and High-Energy Physics Laboratory (LPNHE by its French initials) [PC11] and the University of Washington systems [DAM20]. Figure 5.1 shows a scheme of the LPNHE test chamber apparatus.

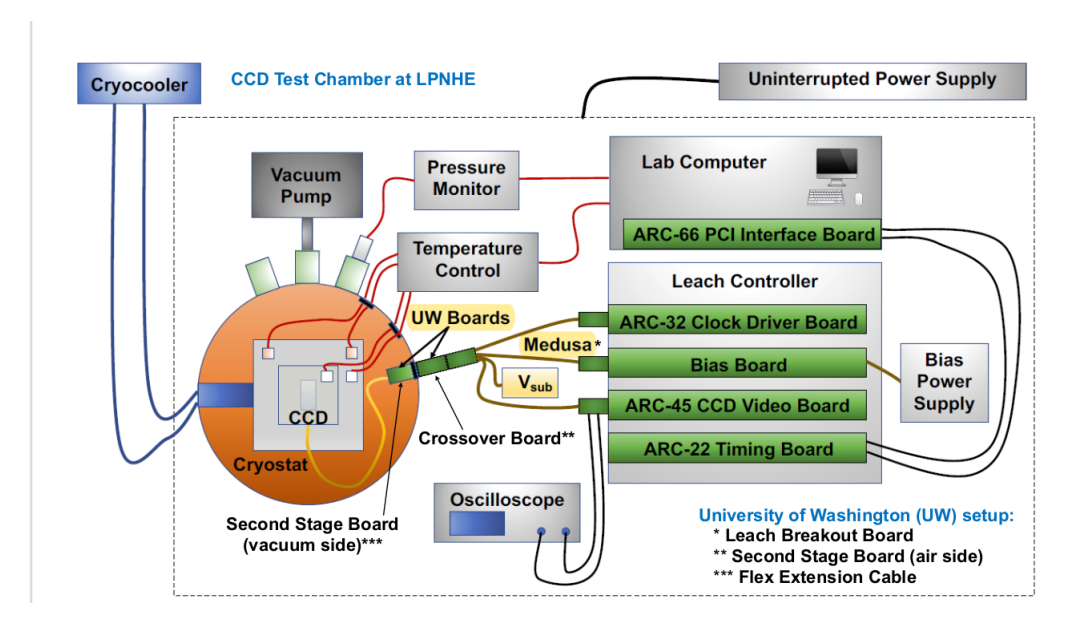


Figure 5.1: Test-chamber apparatus. Retrieved from [PC11].

One of the fundamental elements to get the setup working as the specifications [PC11],

is the cryocooler, which will regulate the temperature and allow for the state it to be a low value. The cryocooler available for the IFCA setup differs from the one at Paris or Washington since it allows a bigger range of temperature (that could go as low as T=20K) but it is much bigger and also works with a piston; it has near 0.5 meters of length and a weight of 13.7kg, however, its size could introduce some problems as vibrations due to the piston and instabilities. In order to reduce the damage in the CCD induced by vibrations, the cryocooler will be fixed by an independent mechanical support system and will be connected to the vacuum chamber (cryostat) as it is showed in the figure 5.2. The system will work with a CCD of $6k \times 1K$ from the University of Washington; the figure 5.3 shows the location of the CCD inside the cryostat. For more details, refer to Appendix E.

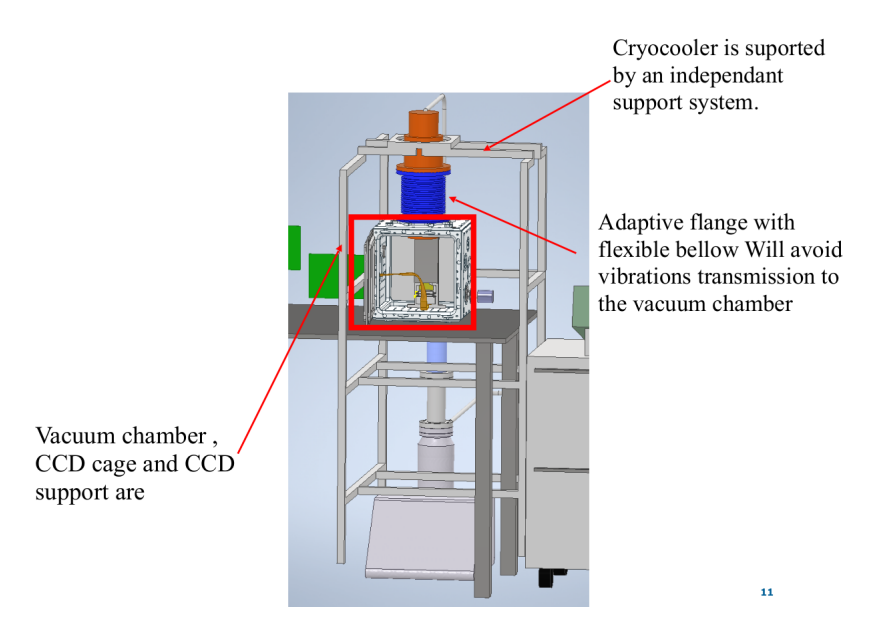


Figure 5.2: Setup system: cryostat envelop at IFCA. Retrieved from [JDR⁺20].

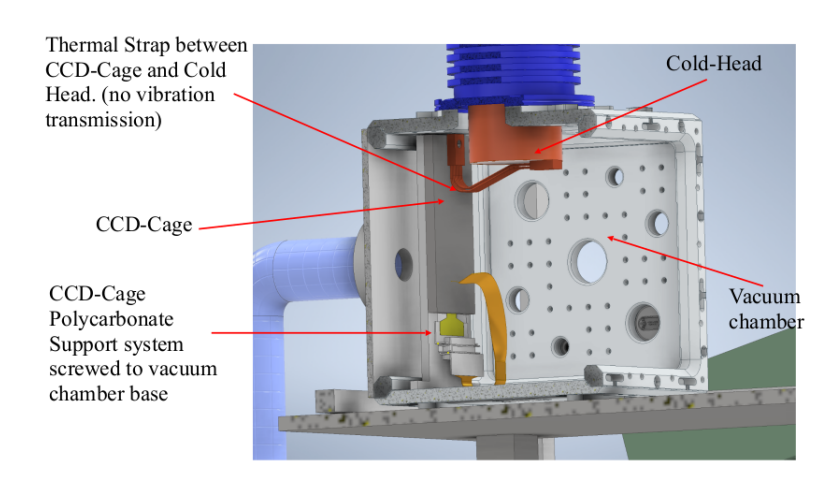


Figure 5.3: CCD setup system inside the cryostat. Retrieved from [Jav20].

5.2 Dark Current analysis

As it was mentioned in Chapter 4, the silicon detector stores the information of the particles which interact with the silicon bulk of the CCD, generating a charge signal that travels through the detector. Since the charge leaves a trace in the detector, it is possible to know certain characteristics of the interaction. The charge signal is transformed into an output voltage, which is stored in an *analog to digital unit* (ADU).

5.2.1 The FITS format

The data obtained at DAMIC and DAMIC-M is stored in a FITS format. The Flexible Image Transport System (FITS) is widely used in astronomy with the purpose of transport, storing and analysis of the data. A FITS image can be composed by either multi-dimensional arrays of data or 2-D data tables made of rows and columns of information. The FITS basic structure consists on Header Data Units (HDUs), which in turn contains a Header Unit (ASCII entries) and a Data Unit (data as an array of binary data or as a table) [GS20]. The FITS format makes it easier to handle and analyse a huge amount of data in a compressed format [PWGT00].

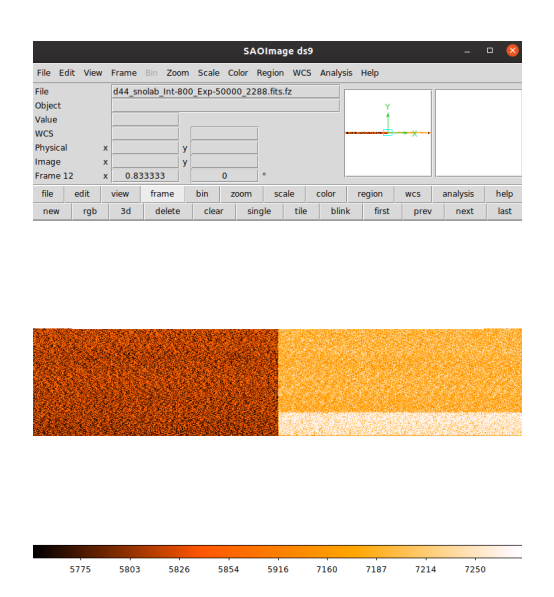


Figure 5.4: Image in FITS format visualised by SAOImage.

The output voltage is stored in an *analog to digital unit* (ADU). Once the data is collected, it can be visualized with different tools; the program employed in this work was SAOImage DS9 [sao]. The figure 5.4 shows an example of an image recorded by DAMIC in 2017, where, among other information, the quantity of pixels, the charge content and its position, the exposure time and the reading time are displayed.

5.2.2 Overscan

The *overscan* regions (thick regions located in the borders of the left and right sides of the figure), are those rows and columns that are not exposed to light, hence those pixels have a

lack of charge (or signal), see figure 5.5.

The analysis is done using raw images which are located according with the DAMIC array, as it was mentioned in section 4.1, the CCDs are assembled in a way that one CCD is "over" the other one. FITS images are read in the same way, the array is like the one showed in the figure 5.6. Recalling that DAMIC is working with seven CCDs, the extensions available for the analysis are: Ext1, Ext2, Ext3, Ext4, Ext6, Ext 11, Ext 12 (here the number associated with each extension is related with the position of the CCD in the array).

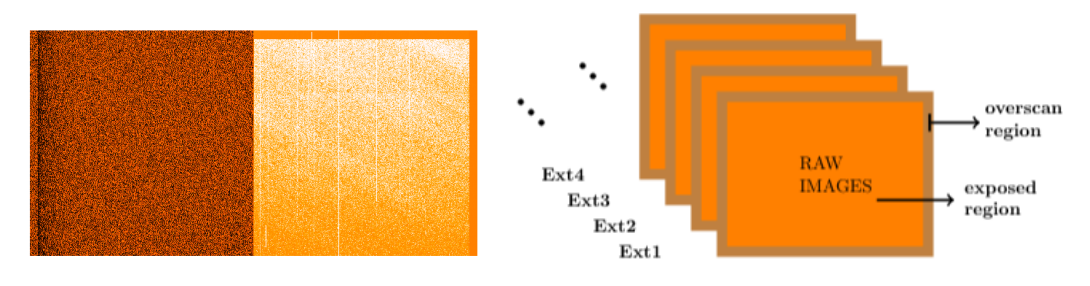


Figure 5.5: Image with overscan

Figure 5.6: FITS images.

Figure 5.7: Left: Example of an image with overscan (darker regions located at the edges of the figure), visualised with the DS9 program. Right: schematic view of an array containing raw FITS images.

Each image was first visualised with the DS9 program, which is an astronomical application for imaging and data visualisation developed in 1990 by Mike Van Hilst and Eric Mandel at the Smithsonian Astrophysical Observatory, Center for Astrophysics, Harvard University [DS920]. This first analysis was made in order to know if it was possible to work with the whole image or if it was necessary to select the regions where the data was deficient; the information about the reading time, the exposition time as well as the dates when the data was recorded could also be extracted with the DS9 program.

Temperature (K)	Configuration	Exp. time (s)	Date
140	1×100	100168	2017-09-27
150	1×100	50157	2017-09-09
160	1×100	7359	2017-11-28
170	1×100	3754	2017-11-28
180	1×1	4141	2017-11-26
220	1×1	1432	2017-11-23

Table 5.1: DAMIC data analysed

The data set handled in this work is presented in the table 5.1, which covers a range of temperatures going from T=140K to T=220K, this is done with the intention of observe the

behaviour of the dark current when both low and high temperatures are considered; besides, this table includes the date when the data was taken, the exposition time of the CCD and also the two different configurations of collection and reading of the pixels explained in Chapter 4 (i.e., 1×1 , and 1×100 configurations).

The Dark Current (DC) is computed by subtracting the x-overscan of the raw image and dividing by the addition of the exposition time and the reading time, multiplied by the pixel area (see Chapter 3, section 3.3.4):

$$dc = \frac{(image - Xoverscan) * cal_{200}}{3.77 * (exptime + rdtime) * areapix}$$
(5.1)

Where *image* refers to the content of pixels of the whole image, whereas *X-overscan* takes into account only the overscan region in the x axis (overscan content in rows) and *areapix* is the area of the pixels read; *exptime* and *rdtime* are the exposition time and the reading time of the CCDs, respectively. The factor $cal_{200}/3.77$ is the calibration factor needed to convert ADUs into electron units.

The overscan is subtracted from the image due to the fact that it contains the information of the CCD when light does not interact with the silicon bulk, hence these pixels disregard the noise generated by such interactions. Though, the overscan includes the noise generated by readout and electronics that are needed to subtract in order to measure only the noise produced due to dark current.

5.2.3 Results

The table 5.2 presents the logarithm of the DC per electron, per millimeter square per second obtained for the different images presented in the table 5.1; as was mentioned in the previous section, each temperature has seven extensions corresponding to each CCD in the DAMIC array.

T(K)	Ext1	Ext 2	Ext3	Ext4	Ext6	Ext11	Ext12
140	-4.58	-3.93	-4.53	-4.58	-4.51	-4.19	-3.58
150	-2.98	-2.02	-3.06	-3.08	-3.07	-2.96	-1.96
160	-1.51	-1.75	-2.04	-1.89	-1.84	-1.70	-1.82
170	-0.47	-0.65	-0.88	-0.76	-0.71	-0.62	-0.72
180	0.69	0.56	0.42	0.48	0.53	0.59	0.52
220	2.68	2.6	2.51	2.55	2.59	2.62	2.57

Table 5.2: log [DC (e/mm2/sc)]

The following plots, from 5.8 to 5.11, present the dark current for each extension in the

table 5.1 vs the temperature, the logarithmic values are taken in order to reflect the linear behaviour of the dark current with temperature. A linear fit was applied to each set of data using R language [R C13]. In the case of the extensions 3, 4, 6 and 11, the linear dependence is more evident for the range of temperatures from T = 150 K to T = 180 K. Whereas, for extensions 1, 2 and 12, the DC is mostly higher than the linear dependence. With regard to figure 5.8, for the extension 1, it can be seen how the DC is higher than the fit for temperatures from T = 160 K to T = 220 K, but for low temperatures (T = 140 K and T = 150 K) the values are below the line. The DC for extension 2 is above the line for all temperatures, except for the lowest value that is T = 140 K.

In the figure 5.9, for both extensions 3 and 4, the DC is under the linear fit for T=220K and T=140K; while its value is higher for temperatures from T=150K to T=180K, except for the extension 4 where the DC is under the line for T=150K, the extensions 6 and 11 (figure 5.10) have this similar behaviour. The extension 12, figure 5.11, has a different performance, since the DC for T=140K, T=160K and T=220K are below the fit, but for T=150K, T=170K and T=180K the DC is above the line.

Finally, the figures 5.12 and 5.13 summarise the behaviour of the DC, i.e., of the data presented in table 5.2. In the figure 5.12 the evolution of the DC for each extension is presented, it can be seen how the amount of DC arises for higher temperatures. The figure 5.13 corresponds to the DC vs the temperature for the seven extensions at the DAMIC array, it can be seen how for extensions 2, 11 and 12 the DC is higher for low temperatures; in the case of high temperatures the DC is very close to the fit. What is more, in the table 5.3 the slopes corresponding to the fit for each extension are presented, the values are around 10 and 13, which is an indication of the linear dependence of the DC with the temperature. In the same figure, the red diamond markers located at T=115K, T=195K and T=255K correspond to measurements done by Chavarria, for higher temperatures his results are close to the fit.

It is important to mention that the linear fit was applied to the whole range of temperatures (this is, from T=140K to T=220K), nevertheless a further step in the study involves the implementation of a more accurate method for computing the DC, it might be through a fit in the charge distribution to each extension and to each temperature.

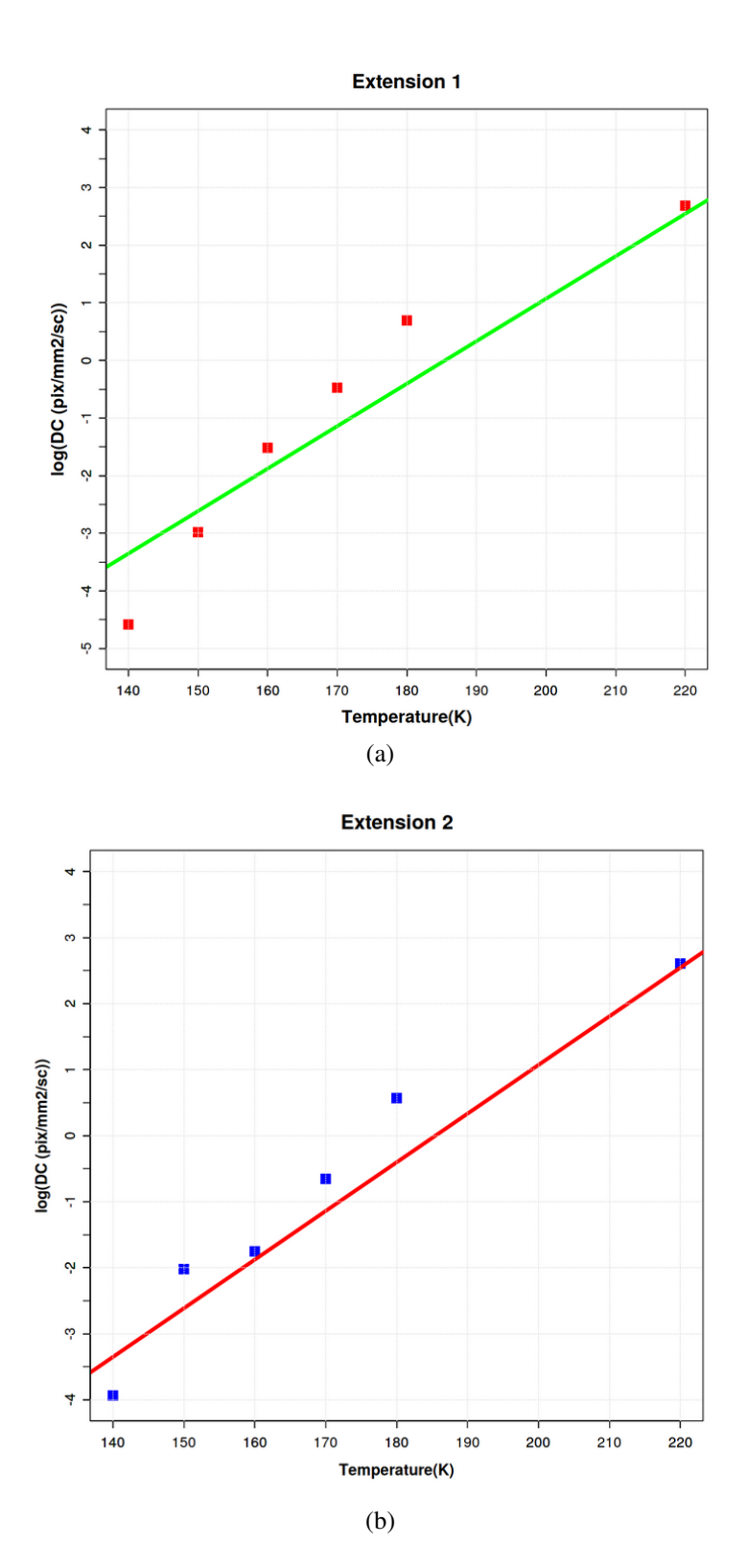


Figure 5.8: Dark Current vs temperature computed for: a) Extension 1 and b) Extension 2

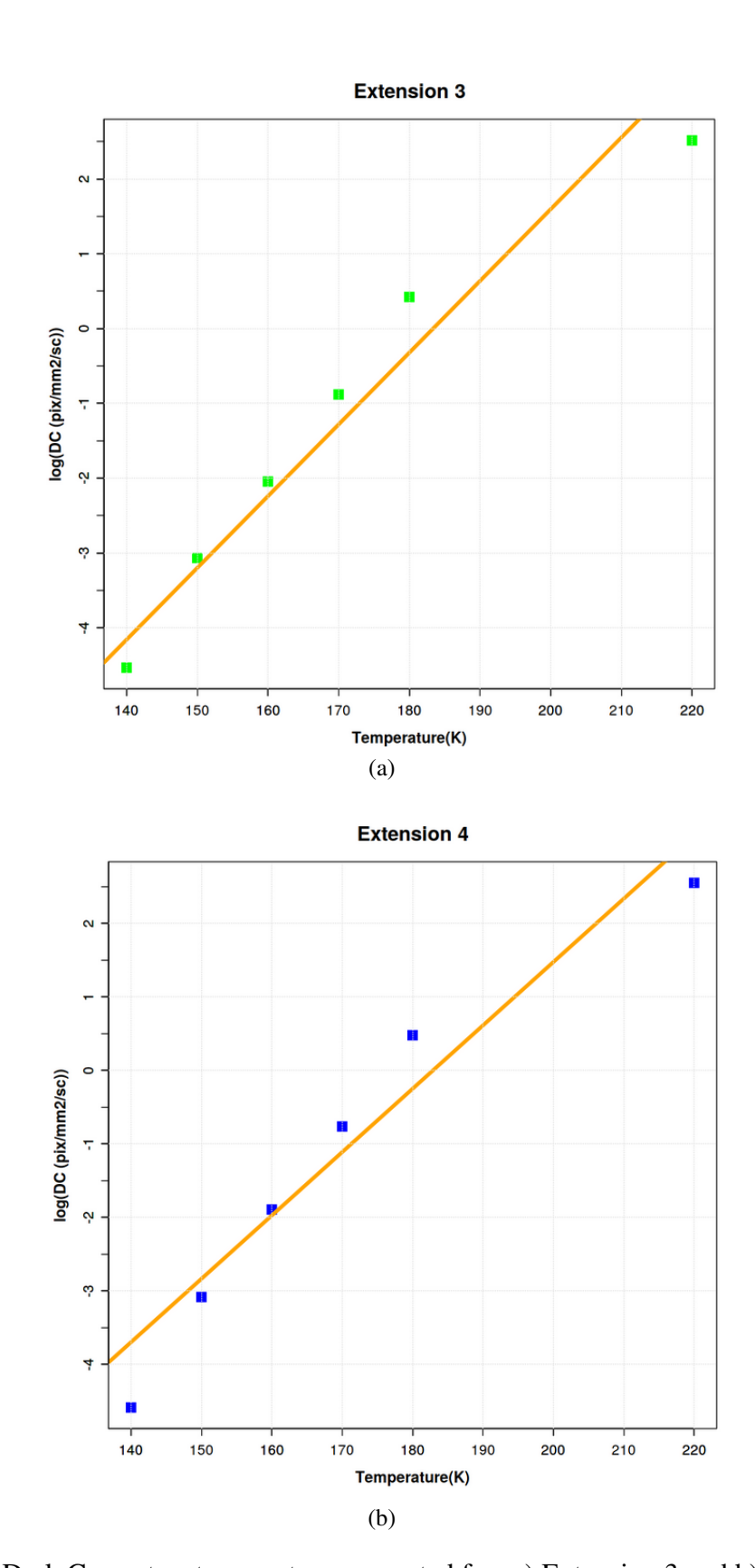


Figure 5.9: Dark Current vs temperature computed for: a) Extension 3 and b) Extension 4

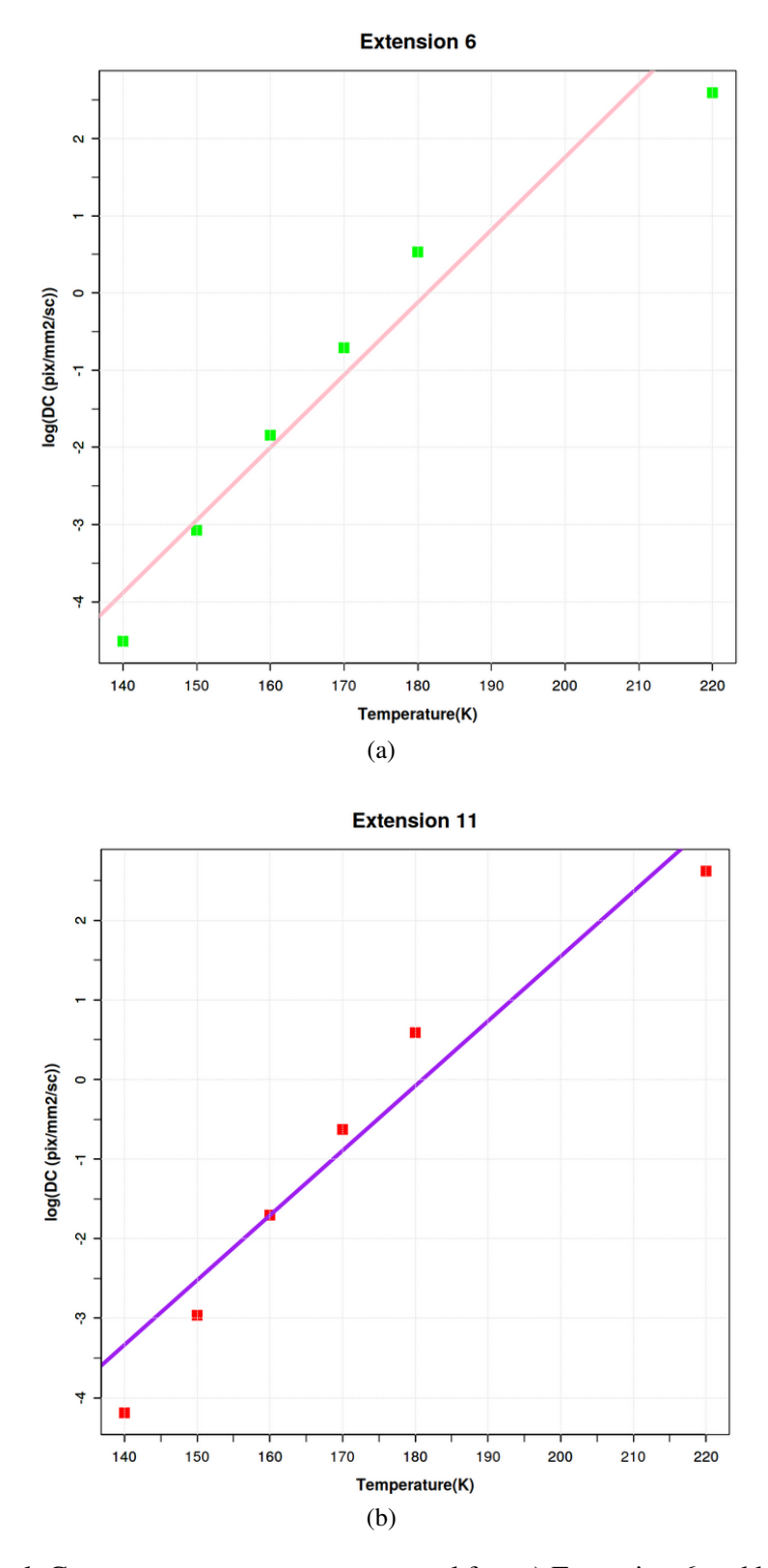


Figure 5.10: Dark Current vs temperature computed for: a) Extension 6 and b) Extension 11

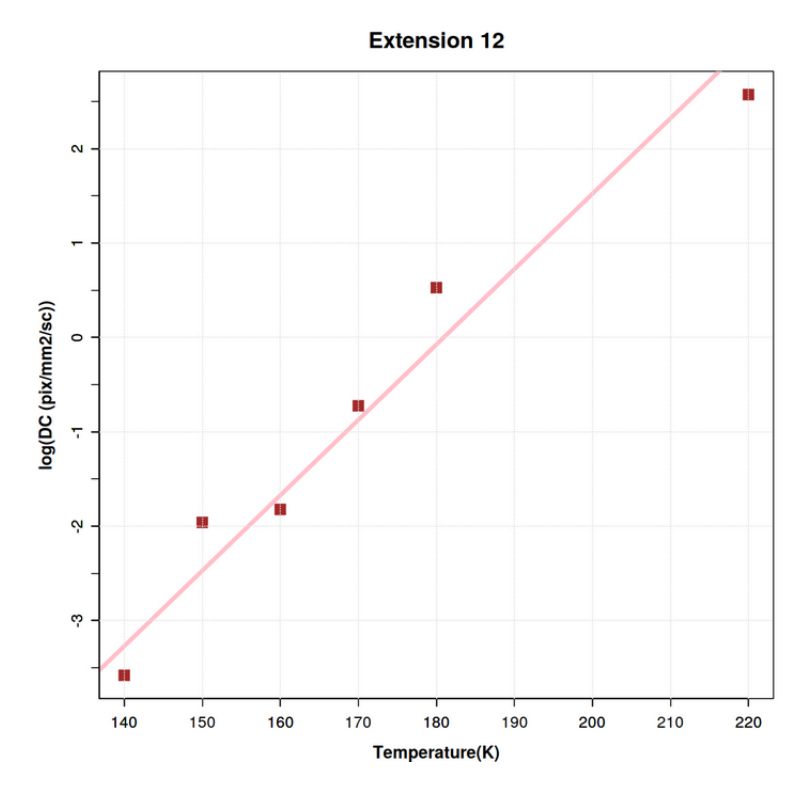


Figure 5.11: Dark Current vs temperature computed for Extension 12

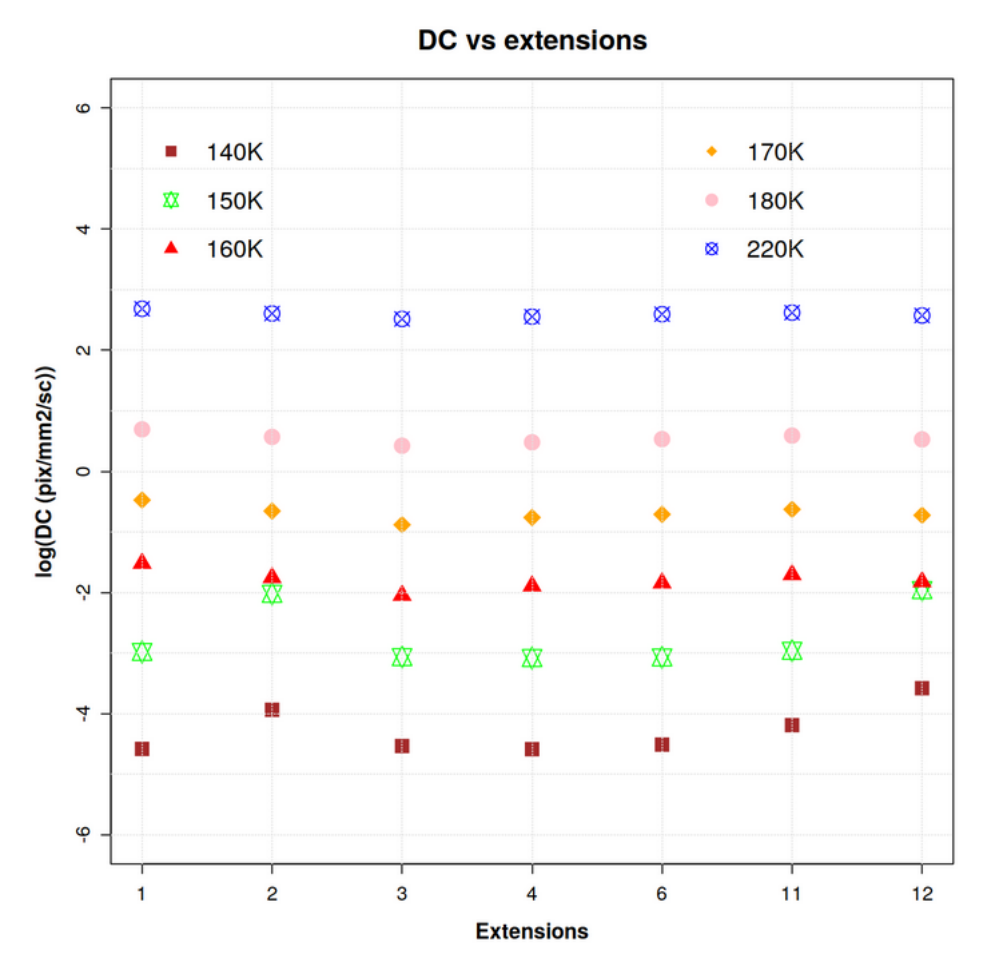


Figure 5.12: Summary 1. Plot of the Dark Current presented in table 5.2 for each extension.

Table 5.3: Slope of the linear fit

Slope
10.6
12.3
11.02
10.87
10.88
11.28
12.95

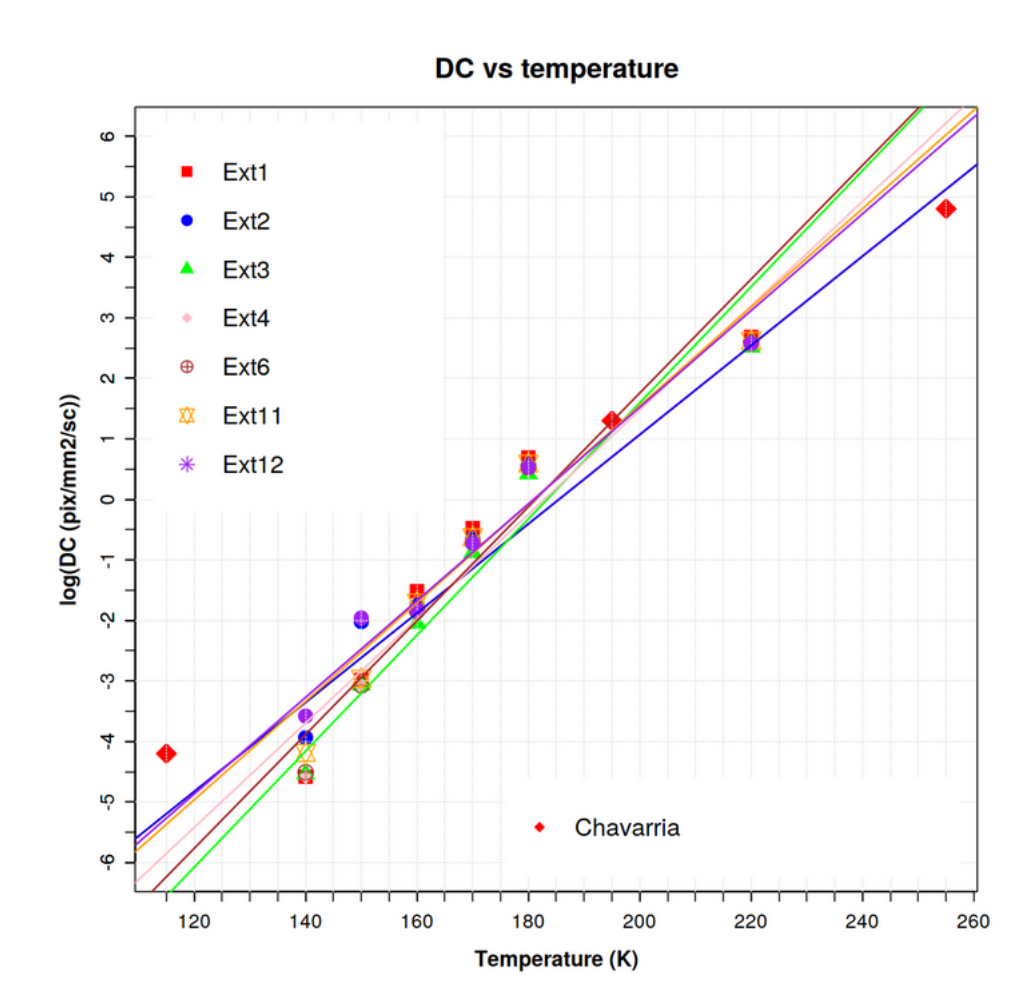


Figure 5.13: Summary 2. Plot of the Dark Current presented in table 5.2 vs temperature, diamond markers at T=115K, 195K and 255K are results measured by Chavarria

Chapter 6

Conclusions

The original goal of this TFM was to assemble the experimental setup for the test-stand CCDs at IFCA in order to start with preliminary studies about the behaviour of the dark current in the arrangement. Unfortunately, due to the coronavirus pandemic, it was infeasible to work at the clean room during the 2019-2020 course.

With the intention to make an initial analysis of dark current in CCDs, data from DAMIC obtained during 2017 was used instead. In summary, the following tasks were carried out:

- A review of the main physical features of silicon semiconductors as particle detectors; making possible the detection of the interaction of incoming particles with the silicon bulk of the semiconductor through elastic collisions.
- Since DAMIC and DAMIC-M, among other experiments, are aimed to search for Dark Matter (DM) candidates in the low mass region, it is important to have accurate measurements of the signals, hence the main sources of noise and damage present in the silicon semiconductors were also listed, making emphasis in the Dark Current (DC)
- One of the main silicon semiconductor detectors employed for the search of DM is the CCD, hence its structure and basic functions were presented in the previous work, Chapter 3, section 3.2.
- A data set obtained at DAMIC during 2017, table 5.1, was analysed in order to observe the dark current dependence on temperature. After the analysis, it was found that the amount of DC depends almost linearly on the temperature, hence for higher temperatures the DC raises too. However, the model could be better if an adjustment on the charge distribution is applied instead. The analysis also implied to work with different programs (such as ROOT, C++, R and DS9).

The DC at low temperature points were intended to be understood with the setup at IFCA, since the experiment at DAMIC-M works at low temperatures, this study could not be done due to the delays originated by the pandemic.

Once the sanitary conditions allows to work physically in the clean room at IFCA, the tasks to be done are the following:

• Work on the test stand CCDs setup.

- Improve the method for calculating the Dark Current and the linear fits.
- Study of systematic of the Dark Current measurements.

ATTACHMENTS

Appendix A

Search of Dark Matter: detection methods

A.1 Indirect detection

Recalling figure 2.3, Indirect Detection (ID) takes into consideration the DM candidate interactions with themselves and self-annihilation producing a cascade of known particles such as neutrinos, e^-e^+ and photons; for the abundance of these particle, galactic centers, dwarf galaxies, clusters of galaxies, the Earth and the Sun are viable targets to look for Dark Matter decays. There are many experiments which use this type of detection [Fre17], some of them are presented in this section.

Agrawal, et al. [ABFH15], studied the Dark Matter annihilation to electroweak bosons and top quarks in the galactic centres; taking as signal gamma rays, the decay product of W, Z, top and Higgs into photons and neutral pions, lead to a radiation final state which can be detected with telescopes. The Fermi Gamma-Ray Space Telescope [AAA+09] has set the strongest limits on the dark matter annihilation cross section at observing dwarf galaxies, achieving a constrain of WIMPs mass lighter than 100 GeV [AAA+15].

A.2 Search at accelerators

As it is shown in figure 2.3, at colliders pair production of DM particles can be achieved in two ways: 1) from the annihilation of SM particles or 2) from interactions that involve a mediator particle between DM and SM particles. Portal models are those where DM particles are added to the SM, here the known particles act as a portal between the DM and SM sectors.

The search of DM particles can take advantage of the search of SUSY at CERN, since the *lightest supersymetric particle* (LSP) predicted by the SUSY model shares the same properties as WIMPs [Dog].

Appendix B

Physics of semiconductors

B.1 The band structure

Given a single atom, the energy of an electron occupying an atomic orbital is quantized, i.e, only discrete values of electron energy are allowed [Nea12]. The probability of finding an electron at a particular distance from the nucleus is given by the probability density function p(r). When two identical atoms are close to each other, the wave functions of the quantum state of each electron overlap, meaning that the electrons interact. This perturbation produce a splitting of the quantized energy level into discrete energy levels. The left side of figure B.1a shows the overlapping radial probability functions for two hydrogen atoms which are in close to each other, while in the right side it is shown how the n=1 state splits due the interaction of the two atoms.

When in a regular periodic arrangement (like in a crystalline solid) atoms are brought together the initial quantized energy level will split into a band of discrete energy levels, as it is shown in figure B.1b where r_0 is the equilibrium interatomic distance in the array. Within the band of allowed energies (which is located at r_0), such energies have discrete levels, it is forbidden for two electrons to have the same quantum number (due to the Pauli exclusion principle), as consequence the discrete energy splits into a band of energies so each electron can occupy a different quantum state.

The continuum electronic energy states in a solid formed due to the close proximity of atoms is known as an *energy band*; while a *bandgap* is a region with no available states

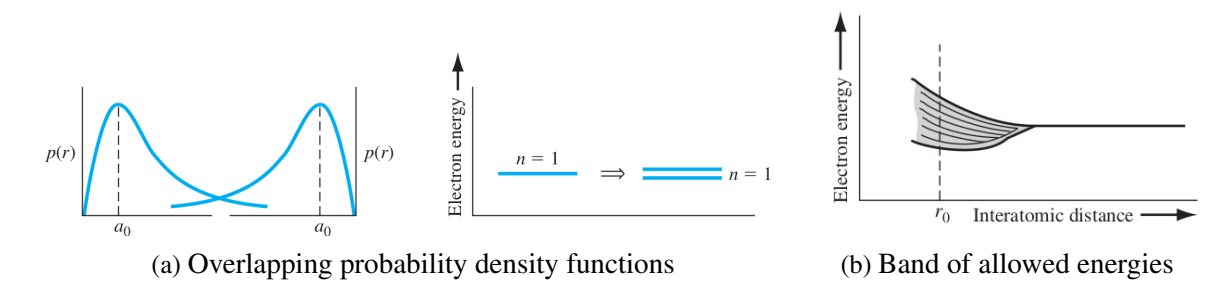


Figure B.1: a) Left side: Probability density functions of two adjacent hydrogen atoms. Right side: splitting of the n=1 state. The x axis indicates the interatomic distance. b) The splitting of an energy state into a band of allowed states for a collection of hydrogen atoms. Retrieved from [Nea12].

[Woo18]. As it is known, materials can be classified into three categories according with their facility to conduct charge: conductors, insulators and semiconductors. These properties are determined by the filling pattern of their energy bands:

- valence band: the highest occupied energy band at temperature of zero kelvin [Neu13]. The energy available in this band is denoted by E_V .
- conduction band: the collection of the lowest vacant electronic states [Woo18]. Electrons from this band contribute to the conductivity of the material. The energy available in this band is denoted by E_C .
- bandgap: the gap between the valence band and the conduction band. The energy available in this band is denoted by E_a , this is the width of the forbidden energy band.
- Fermi level: the energy under which all states are filled with electrons and above which all states are empty at T=0 K. Energy in this level is denoted by E_F [Nea12].

In figure 3.1 it is shown how when the valence band and conduction band overlap, as in the case of metals, the lack of bandgap makes the conduction band to be partially occupied by electrons (even at $T=0~\rm K$) allowing the free movement of electrons and, as consequence, the conduction of charge. Insulators have a large bandgap (consisting on several eV), then the conduction band states are unoccupied at finite temperatures, resulting into a small number of free charge carriers and little conductivity; even for high temperatures (above $T=100~\rm K$) the probability of thermal excitation of an electron into the conduction band is very low.

In the case of semiconductors, the size of the bandgap is such that electrons can be excited into the conduction band at room temperatures. This type of materials are a subgroup of insulators, behaving like conductors at high temperatures and insulators at zero kelvin [Jun11], [Mag18]. This characteristic is what makes of semiconductors a suitable radiation detector. Elements in the VI Group of the Periodic Table are useful semiconductors (such as Si, Ge, Sn), with silicon the most used as detector due to its high abundance and its properties which are presented in the following section.

Appendix C

DAMIC experimental setup

C.1 Readout

Until the readout is performed, the collected charge is held at the gates during hour- to daylong image exposure. Readout consists on the transfer of the charge from one pixel to the next one in y direction along each column through "parallel clocks", while higher frequency clocks move the charge of the last row in the x direction to the CCD's output node where the charge is measured. The inefficiency of the charge transfer is low (10^{-6}) , the readout noise for the charge collected in a pixel is $\sim 2e^-$ [AAAB+16]; since the average energy to create an electron-hole pair in Si is 3.62 eV, this corresponds to ~ 9 eV (figure 4.6a shows the pixel value distribution for readout noise and charge collected). The reconstructed image contains a two-dimensional map projected on the xy plane of all the particle interactions during the exposure of the detector.

The number of dark electrons 1 collected is proportional to the exposure time, and produces a Poissonian noise. The selection of pixels with significant charge is made under the condition of having a pixel value of $5-6\ \sigma$ above the noise level, with the current data, DAMIC can achieve a threshold of $50eV_{ee}$; this value can vary, depending on the number of pixels over which the charge is spread out and on the depth of the interaction. eV_{ee} is the electron-equivalent energy scale associated to the ionization produced by recoiling electrons from the photoabsorption of x rays with known energy [AAAB+16]. The calibrations were done by illuminating the the CCD with x rays from O, Al, Si, Cr, Mn and Fe sources, having as a result a linear dependence between the CCD output and low energy signals [AAAB+16]. The linear calibration constant k is given by:

$$k = \frac{1}{3.77e V_{ee}} \frac{\sigma_l^2}{\mu_l} \tag{C.1}$$

Where μ_l and σ_l^2 are the mean and variance, respectively. Equation C.1 estimates k when few charge carries are collected by a pixel. Figure C.1

¹electrons produced by thermal excitation in the Si substrate

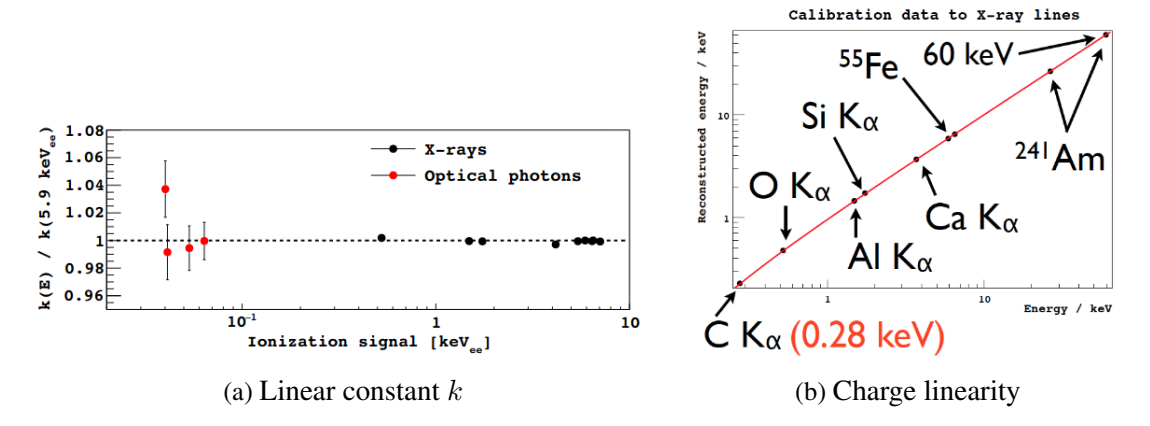


Figure C.1: a) Linear constant k relating the CCD output signal to the ionization generated in the substrate. Calibrations at high energies were performed with x rays, while the lowest energy points were obtained using optical photons. Retrieved from [AAAB⁺16]. b) Linearity of charge collection for DAMIC CCDs. Retrieved from [Lia16].

Appendix D

Expected results from DAMIC and DAMIC-M

DAMIC-M is expected to reach an unprecedented sensitivity to DM-electron scattering, as well as hidden-photon DM, for its capacity to detect signals from the interaction of DM particle with valence electrons. The expected sensitivity of DAMIC-M, with one year exposure, can be seen in figure D.1, where it is compared with other experiments and with theoretical models; right side corresponds to a light dark photon mediator, whereas the left side corresponds to a WIMP-nucleon spin-independent scattering.

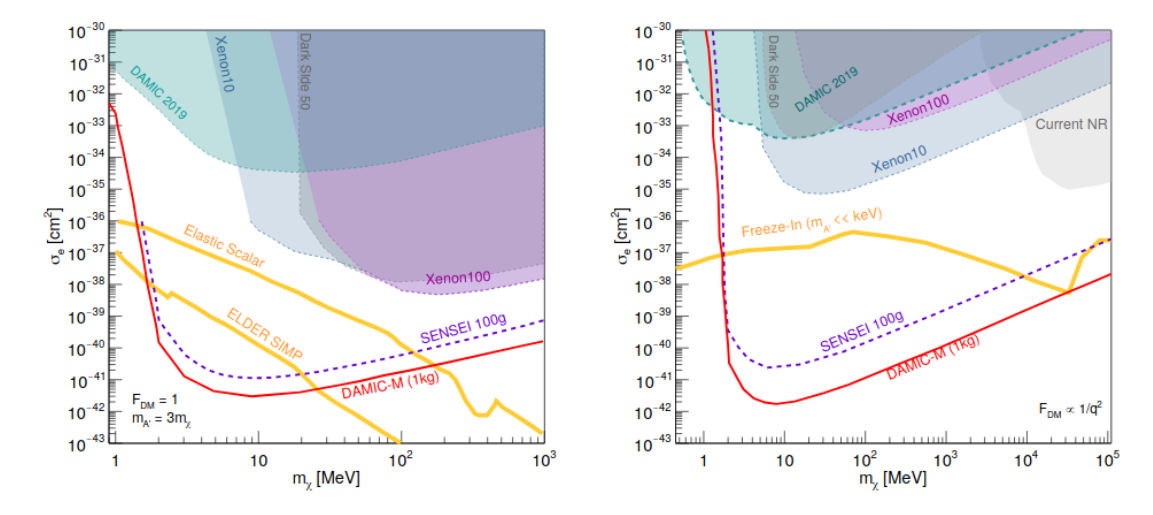


Figure D.1: Left: DM particle scatters through a heavy mediator. Right: DM particle scatters through a light mediator. Retrieved from [Set20].

Appendix E

Test-stand CCDs at IFCA: current status

The action plan for the test-stand CCDs, installed at IFCA, contemplates make the system work, perform both the readout and the calibrations of the signals obtained and measure the level of noise, such as the dark current. Afterwards, the array array will be moved to the Canfranc Underground Laboratory (LSC by its Spanish initials), in order to characterise the radioactive contamination of a new generation of CCDs [JDR⁺20].



Figure E.1: CCDs setup at IFCA Clean Room. Retrieved from [JDR⁺20].

The arrangement of the system, as showed in the figure 5.1, is based on the setup implemented by the LPNHE group [PC11]. The figure E.1 shows the CCDs setup which will be installed at IFCA Clean Room. The model of the CCDs acquired, figure E.2, is UW-1602S. The extension cable includes a skipper CCD.

In the case of figure E.3, the characteristics of the components for the Test stand is presented. Up to September 2020, the vacuum pump and the cryocooler have been delivered, besides the CCD readout system is ready to be tested. In the other hand, the vacuum chamber,



Figure E.2: UW-1602S CCD to be employed at IFCA. Retrieved from [Jav20].

the temperature sensors and heaters, the thermal strap, and the cryocooler support system are still missing.

Vacuum chamber	Ideal Vacuum Products 2x12x12 Cubic Modular
CCD box	Shipping cage
Cryocooler	CH-110 from Sumitomo
Pump	Turbolab 90i
Pressure sensor	Leybold, Penning PTR90
Temperature controller	CTC100: Stanford Research System
Vsub power supply	SMA conector on the Leach Breakout board
Power supplies	ARC-80 (Astronomical Research Cameras)
CCD controller	Leach system (Astronomical Research Cameras + UW boards)
Status	Under construction

Figure E.3: Test stand IFCA components. Retrieved from [Jav20].

References

- [AAA+09] W. B. Atwood, A. A. Abdo, M. Ackermann, W. Althouse, B. Anderson, M. Axelsson, L. Baldini, J. Ballet, D. L. Band, G. Barbiellini, y et al. THE LARGE AREA TELESCOPE ON THEFERMI GAMMA-RAY SPACE TELESCOPEMISSION. *The Astrophysical Journal*, 697(2):1071–1102, May 2009. url: http://dx.doi.org/10.1088/0004-637X/697/2/1071.
- [AAA⁺15] M. Ackermann, A. Albert, B. Anderson, W.B. Atwood, L. Baldini, G. Barbiellini, D. Bastieri, K. Bechtol, R. Bellazzini, E. Bissaldi, y et al. Searching for Dark Matter Annihilation from Milky Way Dwarf Spheroidal Galaxies with Six Years of Fermi Large Area Telescope Data. *Physical Review Letters*, 115(23), Nov 2015. url: http://dx.doi.org/10.1103/PhysRevLett.115. 231301.
- [AAAB⁺16] A. Aguilar-Arevalo, D. Amidei, X. Bertou, M. Butner, G. Cancelo, A. Castañeda Vázquez, B. A. Cervantes Vergara, A. E. Chavarria, C. R. Chavez, J. R. T. de Mello Neto, y et al. Search for low-mass WIMPs in a 0.6 kg day exposure of the DAMIC experiment at SNOLAB. *Physical Review D*, 94(8), Oct 2016. url: http://dx.doi.org/10.1103/PhysRevD.94.082006.
- [AAAB+20] A. Aguilar-Arevalo, D. Amidei, D. Baxter, G. Cancelo, B. A. Cervantes Vergara, A. E. Chavarria, J. C. D'Olivo, J. Estrada, F. Favela-Perez, R. Gaior, Y. Guardincerri, E. W. Hoppe, T. W. Hossbach, B. Kilminster, I. Lawson, S. J. Lee, A. Letessier-Selvon, A. Matalon, P. Mitra, C. T. Overman, A. Piers, P. Privitera, K. Ramanathan, J. Da Rocha, Y. Sarkis, M. Settimo, R. Smida, R. Thomas, J. Tiffenberg, M. Traina, R. Vilar, y A. L. Virto. Results on low-mass weakly interacting massive particles from a 11 kg-day target exposure of DAMIC at SNOLAB, 2020.
- [ABFH15] Prateek Agrawal, Brian Batell, Patrick J. Fox, y Roni Harnik. WIMPs at the galactic center. *Journal of Cosmology and Astroparticle Physics*, 2015(05):011–011, May 2015. url: http://dx.doi.org/10.1088/1475-7516/2015/05/011.

- [And20] Erik; et al. Andersson. Projected sensitivity to sub-GeVdark matter of next-generationsemiconductor detectors. *JCAP*, 05:18, 2020.
- [BCD+12] J. Barreto, H. Cease, H.T. Diehl, J. Estrada, B. Flaugher, N. Harrison, J. Jones, B. Kilminster, J. Molina, J. Smith, y et al. Direct search for low mass dark matter particles with CCDs. *Physics Letters B*, 711(3-4):264–269, May 2012. url: http://dx.doi.org/10.1016/j.physletb.2012.04.006.
- [BH18] Gianfranco Bertone y Dan Hooper. History of dark matter. *Reviews of Modern Physics*, 90(4), Oct 2018. url: http://dx.doi.org/10.1103/RevModPhys. 90.045002.
- [Blo17] Ita; et al. Bloc. Searching for dark absorption with direct detection experiments. *J. High Energ. Phys*, 87:18, 2017.
- [Cav] C Cavadore. EEV Report. https://www.eso.org/sci/facilities/develop/detectors/optdet/docs/reports/EEV-report.html.
- [CM20] N. Castelló-Mor. DAMIC-M experiment: Thick, silicon CCDs to search for light dark matter. *Nuclear Instruments and Methods in Physics Research Section A: Accelerators, Spectrometers, Detectors and Associated Equipment*, 958:162933, Apr 2020. url: http://dx.doi.org/10.1016/j.nima.2019.162933.
- [CTAA⁺14] Alvaro Chavarria, Javier Tiffenberg, Alexis Aguilar-Arevalo, Dan Amidei, Xavier Bertou, Gustavo Cancelo, Juan Carlos D'Olivo, Juan Estrada, Guillermo Fernandez Moroni, Federico Izraelevitch, Ben Kilminster, Yashmanth Langisetty, Junhui Liao, Jorge Molina, Paolo Privitera, Carolina Salazar, Youssef Sarkis, Vic Scarpine, Tom Schwarz, Miguel Sofo Haro, Frederic Trillaud, y Jing Zhou. DAMIC at SNOLAB, 2014.
- [DAM20] DAMIC@UW. DAMIC at SNOLAB. https://www.npl.washington.edu/damic/description, Mayo 2020.
- [DM20] DAMIC-M. Dark Matter In CCDS at Modane. https://damic.uchicago.edu/detector.php#paragraph211, Mayo 2020.
- [Dog] Tovey, D. Doglioni, C. Searching for Dark Matter with the ATLAS detector. url: https://atlas.cern/updates/atlas-feature/dark-matter.
- [DS84] A. Drukier y L. Stodolsky. Principles and applications of a neutral-current detector for neutrino physics and astronomy. *Phys. Rev. D*, 30:2295–2309, Dec 1984. url: https://link.aps.org/doi/10.1103/PhysRevD.30.2295.

- [DS920] SAOImageDS9: An image display and visualization tool for astronomical data. https://sites.google.com/cfa.harvard.edu/saoimageds9/, 2020. Accessed: 2020-05-20.
- [eaPC14] Ade PAR et al (Planck Collaboration). Planck2013 results. I. Overview of products and scientific results. *Astronomy and Astrophysics*, 571(A1):48, 2014.
- [FGL20] Marco Fabbrichesi, Emidio Gabrielli, y Gaia Lanfranchi. The Dark Photon, 2020.
- [Fre17] Katherine Freese. Status of dark matter in the universe. *International Journal of Modern Physics D*, 26(06):1730012, Mar 2017. url: http://dx.doi.org/10.1142/S0218271817300129.
- [GS20] Damke Guillermo y Majewski Steve. The FITS Image Format and Image Display with DS9, May 2020.
- [GW85] Mark W. Goodman y Edward Witten. Detectability of certain dark-matter candidates. *Phys. Rev. D*, 31:3059–3063, Jun 1985. url: https://link.aps.org/doi/10.1103/PhysRevD.31.3059.
- [Jan01] J.R. Janesick. *Scientific Charge-coupled Devices*. Press Monograph Series. Society of Photo Optical, 2001. url: https://books.google.es/books?id=rkgBkbDie7kC.
- [Jav20] Gonzalez Javier. DAMIC CCD readout overview, Sep 2020.
- [JDR⁺20] Gonzalez F. Javier, Moya D., Jaramillo R., Lantaron A., Castello N., Virto A., Vila I, y Vilar R. Test-stand CDDs at IFCA overview, Sep 2020.
- [JL20] S. Juhyung Lee. Lecture notes in "Dark Matter in CCDs at Modane (DAMIC-M): a silicon detector apparatus searching for low-energy physics processes". https://indico.cern.ch/event/813597/contributions/3727832/attachments/1988413/3314169/7_SJL_2020_02_17_TREDI2020_DAMICM_Talk.pdf, February 2020.
- [Jun11] Alexandra Junkes. *Influence of radiation induced defect clusters on silicon particle detectors*. PhD thesis, Hamburg U., 2011.
- [Lan74] D. V. Lang. Deep-level transient spectroscopy: A new method to characterize traps in semiconductors. *Journal of Applied Physics*, 45(7):3023–3032, 1974. url: https://doi.org/10.1063/1.1663719.

- [Lia16] Junhui Liao. Low Mass WIMP Detection with CCDs, 2016. url: https://doi.org/10.5167/uzh-127064.
- [LR12] Claude Leroy y Pier-Giorgio Rancoita. *Silicon solid state devices and radiation detection*. World Scientific, Hackensack, USA, 2012.
- [Mag18] Débora Magalhães. Study and Characterization via Monte Carlo Simulation of Ionizing Radiation Damages in Hybrid Pixel Detectors. PhD thesis, 05 2018.
- [Mar17] Alberto Belloni Aaron Chou Priscilla Cushman Bertrand Echenard Marco Battaglieri, et al. US Cosmic Visions: New Ideas in Dark Matter 2017: Community Report, 2017.
- [Mol99] Michael Moll. Radiation damage in silicon particle detectors: Microscopic defects and macroscopic properties. PhD thesis, Hamburg U., 1999.
- [Nea12] D. A. Neamen. *Semiconductor Physics And Devices*. McGraw-Hill Education Europe, 2012.
- [Neu13] Coralie Neubüser. Impact of Irradiations by Protons with different Energies on Silicon Sensors. Master's thesis, Hamburg U., 2013.
- [PC11] Guy Julien Toussenel Francois Laforge Bertrand Levy Jean-Michel Cossin Isabelle Pain, Reynald y Violaine Cardot. Nuclear and high-energy physics laboratory LPNHE. Activity report 2008-2009, 2011.
- [Pee93] P. J. E. Peebles. *Principles of physical cosmology*. Princeton Univserity, 1993.
- [Pow16] Andrew J. Powell. *The cosmology and astrophysics of axion-like particles*. PhD thesis, Oxford U., 2016.
- [PWGT00] William Pence, R. White, P. Greenfield, y Douglas Tody. A FITS Image Compression Proposal. 216:551, 01 2000.
- [R C13] R Core Team. *R: A Language and Environment for Statistical Computing*. R Foundation for Statistical Computing, Vienna, Austria, 2013. url: http://www.R-project.org/.
- [Red19] Javier Redondo. Alternative dark matter candidates: axions and ALPs. *PoS*, NOW2018:083, 2019.
- [RF70] Vera C. Rubin y Jr. Ford, W. Kent. Rotation of the Andromeda Nebula from a Spectroscopic Survey of Emission Regions., 159:379, Febrero 1970.

- [sao] SAOImage DS9. https://sites.google.com/cfa.harvard.edu/saoimageds9/about?authuser=0.
- [Set20] Mariangela Settimo. Search for low-mass dark matter with the DAMIC experiment, 2020.
- [SNO06] SNOLAB. *User's Handbook*. Rev. 2, 2006.
- [Spi05] H. Spieler. *Semiconductor Detector Systems*. Series on Semiconductor Science and Technology. OUP Oxford, 2005. url: https://books.google.es/books?id=MUMb3y37yqYC.
- [Sze12] S.M. Sze. *Semiconductor Devices: Physics and Technology*. John Wiley & Sons Singapore Pte. Limited, 2012.
- [TSHDW⁺17] Javier Tiffenberg, Miguel Sofo-Haro, Alex Drlica-Wagner, Rouven Essig, Yann Guardincerri, Steve Holland, Tomer Volansky, y Tien-Tien Yu. Single-Electron and Single-Photon Sensitivity with a Silicon Skipper CCD. *Physical Review Letters*, 119(13), Sep 2017. url: http://dx.doi.org/10.1103/PhysRevLett.119.131802.
- [van63] V. A. J. van Lint. Mechanisms of Transient Radiation Effects. *IEEE Transactions on Nuclear Science*, 10(5):11–19, 1963.
- [WBW⁺02] Ralf Widenhorn, Morley Blouke, Alexander Weber, Armin Rest, y Erik Bodegom. Temperature dependence of dark current in a CCD. *Proceedings of SPIE The International Society for Optical Engineering*, 4669, 04 2002.
- [Woo18] Daniel Wood. Radiation-induced Depp-Level Defects in CCD Imaging and Spectroscopy Sensors. Master's thesis, PhD thesis The Open University, 2018.

Este documento fue editado y tipografiado con LAT_EX empleando la clase **esi-tfg** (versión 0.20181017) que se puede encontrar en: https://bitbucket.org/esi_atc/esi-tfg